Enhanced Conformal Perfectly Matched Layers for Bernstein-Bézier Finite Element Modelling of Short Wave Scattering

A. El Kacimi[1], O. Laghrouche[2], D. Ouazar[3], M.S. Mohamed[2], M. Seaid[4], and J. Trevelyan[4]

[1]Laboratory of Modeling and Combinatorial, FP Safi, Cadi Ayyad University, Morocco
[2]Institute for Infrastructure and Environment, Heriot-Watt University, Edinburgh EH14 4AS, UK
[3]Mohammed VI Polytechnic University, Hay My Rachid, 43150 Ben Guerir, Morocco
[4]Department of Engineering, Durham University, Durham DH1 3LE, UK

Abstract

The aim of this paper is to accurately solve short wave scattering problems governed by the Helmholtz equation using the Bernstein-Bézier Finite Element method (BBFEM), combined with a conformal perfectly matched layer (PML). Enhanced PMLs, where curved geometries are represented by means of the blending map method of Gordon and Hall, are numerically investigated. In particular, the performance of radial and elliptical shaped PMLs, with a parabolic absorption function, are assessed and compared in terms of accuracy against second order Bayliss-Gunzburge-Turkel (BGT_2) based local absorbing boundary conditions. Numerical results dealing with problems of Hankel source radiation and wave scattering by a rigid cylinder show that the radial shaped PML, with the h and p versions of BBFEM, enables the recovery of the predicted algebraic and exponential convergence rates of a high order finite element method (FEM). Furthermore, radial shaped BGT_2 and PML have a similar performance, as long as the wave is not sufficiently well resolved. But, BGT_2 performs poorly as the wave resolution increases. Additionally, the effect of harmonics of higher modes on accuracy is examined. The study reveals that the PML outperforms BGT_2 for almost all propagating modes. However, a similar performance is achieved with both methods either with higher modes or a low wave resolution. Results from a multiple scattering benchmark problem provide evidence of the good performance of the proposed PMLs and the benefit of elliptical shaped PMLs in reducing significantly the size of the computational domain, without altering accuracy. The choice of the PML parameters ensuring optimal performance is also discussed.

Keywords. Finite elements; Bernstein-Bézier; Helmholtz equation; absorbing boundary condition; perfectly matched layer; high frequency

1 Introduction

The numerical modelling of wave scattering problems in unbounded media, based on domain discretisation procedures such that the FEM, requires the truncation of the infinite domain and prescription of an appropriate boundary condition allowing outgoing waves to leave the computational domain without spurious reflection.

Two different approaches are commonly used for dealing with domain truncation: either to truncate the domain of the original problem by introducing an absorbing boundary condition (ABC) at the truncation interface or to truncate by introducing an absorbing layer. Among the latter is the

perfectly matched layer (PML), introduced by Bérenger in [1] as a reflectionless absorbing material surrounding the domain of interest. Initially designed for electromagnetic waves, the PML exhibits attractive features that have motivated its extension to a wide range of applications in acoustic scattering (see the survey [2] and references therein), seismology [3–5], elastodynamics [6–9] and geophysical fluid dynamics [10, 11].

ABCs can be broadly classified into two main categories: local or non local, where locality is in the sense that the field at any point on the outer boundary depends only on the fields local to that point. Local ABCs have the advantage to preserve the computational efficiency of the FEM. These include those of Bayliss, Gunzburger and Turkel [12, 13], Engquist and Majda [14, 15], and Feng [16]. Despite the ease of implementation of the lowest order ABCs, acceptable accuracy cannot be obtained unless the artificial boundary is placed far enough from the scatterer [17]. High order ABCs allow one to achieve good accuracy [18–20], but they require a substantial computational effort and are difficult to implement. For a survey about ABCs, see Reference [21]. Non local ABCs such as the truncated Dirichlet-to-Neumann (DtN) [16, 17] enable the artificial boundary to be placed closer to the scatterer, but they yield a dense sub-block in the FE global matrix near the outer boundary. This makes the solution processing of the resulting linear system computationally expensive, especially in 3D applications. For further discussions about ABCs, the reader is directed to References [21, 22]. Alternatively, other techniques have been developed for this purpose, such as the continued-fraction ABC [23], the double absorbing boundary method [24], infinite elements [25, 26], wave envelope [27] and boundary element methods [28, 29].

The main feature of the PML is that it shares the advantage of non local ABCs, because it can be set closer to the scatterer. Furthermore, as for the local ABCs, it preserves the computational efficiency of the FEM. Unfortunately, the PML is no longer reflectionless at the discrete level, resulting in spurious reflections of outgoing waves that may pollute the solution in the entire computational domain. This source of error can be hopefully attenuated by adjusting the FE discretisation and PML parameters. There is extensive literature dealing with the PML and extensions of this concept to more general geometries and applications. Most PML developments make use of straight or planar artificial boundaries and Cartesian coordinates. However, for certain problems, the derivation of PMLs in other coordinate systems is of a relevant importance. Time domain computations of electromagnetic waves in [30], have shown that corner regions are a dominant source of reflection errors. Besides, a noteworthy analysis performed in [31] has indicated that an inadequate choice of the time step may induce long time instabilities of Cartesian PMLs. Based on the complex coordinate stretching approach [32], the Cartesian PML was extended to cylindrical and spherical coordinates in [33–35]. A theoretical study of the PML in curvilinear coordinates was carried out in [36], and optimal PML parameters leading to the best performance were investigated in [37]. A comparative study of the performance of an ellipsoidal PML against infinite elements for Helmholtz problems has been conducted in [38]. The advantages of PML over the infinite element approach in terms of scalability and iteration count of a domain decomposition Helmholtz based solver were demonstrated. A parameter-free PML relying on singular absorbing functions was introduced and studied in [39, 40]. In the time harmonic framework, PML methods involving convex shaped geometries were dealt with in [35, 41–43].

Another problem arising for such applications, in mid and high frequency regimes, is related to the pollution error [44–46]. Standard discretisation methods are unable to solve wave problems at high wavenumbers, because they require a prohibitive computational effort in order to resolve the wave and control the pollution error. High order polynomial methods such as those relying on integrated Legendre [47, 51, 52], Bernstein [47, 53] shape functions and spectral element [47, 54] allow the reduction of the pollution effect, and hence to cope with frequency limitation and high grid resolution requirements of conventional FEMs. Unlike Lagrange polynomials, conventional

hierarchical H_1-conforming p-FEs and Bernstein polynomials are not interpolatory. For p-adaptive FE applications, hierarchical bases are often preferred. As it was first pointed out in [55], the choice of higher-order polynomial shape functions can dramatically affect the conditioning of the FE global matrix. In Reference [47], Bernstein shape functions are demonstrated to be superior when using Krylov subspace iterative solver, compared to spectral FEs and integrated Legendre polynomials. Besides, it has been shown in [48–50] that Bernstein-Bézier FEs over simplicial domains, hexahedra and pyramids can deliver optimal complexity for the standard FE spaces. Comparative studies, dealing with several benchmarks related to Helmholtz problems, against high order wave based methods in [51, 53], have indicated that integrated Legendre and Bernstein-Bézier FEs are able to yield comparable, and even better performance in terms of accuracy and memory requirements. These last two works make use of a Robin type boundary condition enforcing the analytical solution, and accordingly allowing to avoid the problem of truncation of the infinite domain. Using the p-version of these methods for wave problems with smooth solutions, good quality results can be achieved with low numbers of degrees of freedom (DOF) per wavelength [51–53]. On the other hand, it has been shown in [56, 57] that the hp-FEM can control the pollution error by increasing the polynomial order slowly with the wavenumber.

In the present work, a conformal PML is applied as a domain truncation procedure for Bernstein-Bézier finite element computation, to accurately solve short wave scattering problems. The PML is derived in curvilinear coordinates based on complex coordinate stretching [32]. This consists of a simple change of variables, where the spatial coordinates inside the PML are mapped onto the complex space by means of a stretching function. To further enhance the proposed curvilinear PML, the linear blending map method due to Gordon and Hall is adopted [58–60]. Much effort has been spent on optimizing the PML parameters to obtain optimal performance [37, 61, 62]. Polynomial absorption functions are commonly used in order to ensure a progressive attenuation of the outgoing waves in the layer. With this choice, the PML involves free parameters that need to be adjusted in advance by expensive computational procedures. Numerical experiments carried out in this study, dealing with wave scattering problems, reveal that the conclusions of the previous analyses, regarding the optimization of the PML parameters, cannot be extrapolated to high order FEMs. Indeed, based on a parabolic absorption function and radial or elliptical shaped PMLs combined with BBFEM, accurate results can be achieved, with a low computational cost, by enforcing a rapid attenuation of outgoing waves in the artificial layer.

This paper is organized as follows: Section 2 describes the model problem. The PML formulation in curvilinear coordinates is presented in Section 3. An overview of the linear blending map method of Gordon and Hall is given in Section 4. Section 5 is devoted to the FE based Bernstein-Bézier discretisation. The performance of radial and elliptical shaped PMLs, in terms of accuracy, is investigated in Section 6 and compared against those of BGT_2 based ABCs, through three benchmarks. Finally some concluding remarks are drawn in Section 7.

2 The model problem

Let D be a bounded domain in $\mathbb{R}^2$. The sound-hard scattering problem of an incident plane wave u_{in} by an obstacle D consists of finding a function $u : D^c \to \mathbb{C}$ satisfying

$$\begin{cases} -k^2 u - \Delta u = 0, & \text{in} \quad D^c \qquad (2.1a) \\ \boldsymbol{\nabla} u \cdot \boldsymbol{n} = g, & \text{on} \quad \Gamma_D \qquad (2.1b) \\ \lim\limits_{r\to\infty} r^{\frac{1}{2}} \left(\dfrac{\partial u}{\partial r} - \mathrm{i}ku \right) = 0, & \text{uniformly in } \tilde{\boldsymbol{x}}, \qquad (2.1c) \end{cases}$$

where $D^c = \mathbb{R}^2 \setminus D$, g $(= -\boldsymbol{\nabla} u_{\text{in}} \cdot \boldsymbol{n})$ is the prescribed boundary data in $L^2(\Gamma_D)$, $\boldsymbol{n}$ is the outward normal unit vector to Γ_D, $r = |\boldsymbol{x}|$, $|\cdot|$ is the usual l_2 norm, and $\tilde{\boldsymbol{x}} = \frac{\boldsymbol{x}}{r}$.

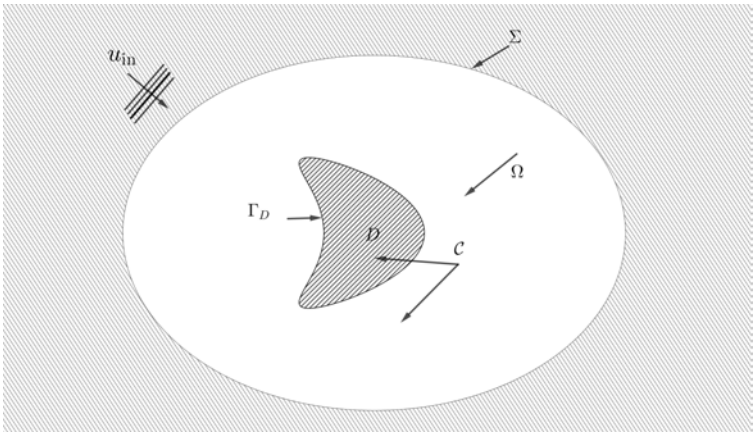

Figure 1: Setup of the wave scattering problem: a hard obstacle D surrounded by an artificial boundary Σ.

The Sommerfeld radiation condition (2.1c) states that the energy is propagating from the obstacle D towards infinity. Here, the time dependence is assumed to be $\exp(-\mathrm{i}\omega t)$. For the unique solvablity of the scattering problem (2.1), see for instance [63].

Suppose one attempts to solve Problem (2.1) in the vicinity of the scatterer, using FEM. Truncating an infinitely large solution domain into a finite computational domain is one of the major difficulties faced when solving open-region wave problems. Both ABCs and PMLs have been widely used as procedures for mesh truncation in this context. Let $\mathcal{C}$ be a convex domain with a piecewise smooth boundary Σ such that $D \subset \mathcal{C}$ (see Figure 1). The imposed ABC on the artificial boundary Σ, should prevent reflections of outgoing waves into the domain $\Omega = \mathcal{C} \setminus D$. The idea of the PML approach consists first in surrounding the computational domain Ω by an artificial layer denoted Ω_{pml} that has minimal reflection and strong absorption properties. The computational domain Ω is next extended to the introduced layer. Further details on the PML are given in the following Section.

3 PML formulation

Let us consider an orthogonal system of curvilinear coordinates (ζ_1, ζ_2) defined in the layer Ω_{pml} (see Figure 2). The location of a point $\boldsymbol{x} = \boldsymbol{x}(\zeta_1, \zeta_2)$ in Ω_{pml} is obtained by intersecting curves parallel and perpendicular to the interface Σ. Since $\mathcal{C}$ is assumed to be convex, the orthogonal projection of $\boldsymbol{x}$ denoted by $\boldsymbol{p}$ onto the interface Σ is well defined. The coordinate ζ_1 is given by the distance from $\boldsymbol{x}$ to $\boldsymbol{p}$, while the coordinate ζ_2 is chosen as a local parametrization of the interface Σ with its arc length. The unit outward normal $\boldsymbol{n} = \boldsymbol{n}(\zeta_2)$ and tangent $\boldsymbol{t} = \boldsymbol{t}(\zeta_2)$ are such that the well known Frenet Formulas hold

$$\frac{\mathrm{d}\boldsymbol{p}}{\mathrm{d}\zeta_2} = \boldsymbol{t} \quad \text{and} \quad \frac{\mathrm{d}\boldsymbol{n}}{\mathrm{d}\zeta_2} = \kappa \boldsymbol{t}, \tag{3.1}$$

where $\kappa = \kappa(\zeta_2)$ is the curvature of Σ at the point $\boldsymbol{p} = \boldsymbol{p}(\zeta_2)$. Any point $\boldsymbol{x}$ in the layer Ω_{pml} can be written as

$$\boldsymbol{x}(\zeta_1, \zeta_2) = \zeta_1 \boldsymbol{n}(\zeta_2) + \boldsymbol{p}(\zeta_2). \tag{3.2}$$

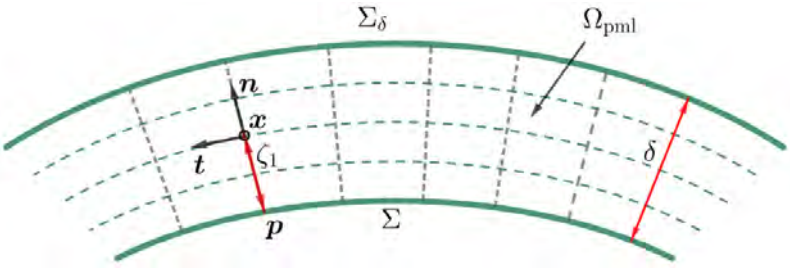

Figure 2: Orthogonal curvilinear coordinates system.

This system of coordinates has been used for PMLs in [35,41,64] and ABCs in [65]. By denoting with l_Σ the length of the artificial boundary Σ, a conformal PML can be defined by

$$\Omega_{\text{pml}} = \{\boldsymbol{x} = \boldsymbol{x}(\zeta_1, \zeta_2) : 0 \leq \zeta_1 < \delta \quad \text{and} \quad 0 \leq \zeta_2 \leq l_\Sigma\}, \tag{3.3}$$

such that $\partial\Omega_{\text{pml}} = \Sigma \cup \Sigma_\delta$ and $\Sigma \cap \Sigma_\delta = \emptyset$, where

$$\Sigma \quad = \quad \{\boldsymbol{x} = \boldsymbol{x}(\zeta_1, \zeta_2) : \zeta_1 = 0 \quad \text{and} \quad 0 \leq \zeta_2 \leq l_\Sigma\} \tag{3.4}$$

and

$$\Sigma_\delta \quad = \quad \{\boldsymbol{x} = \boldsymbol{x}(\zeta_1, \zeta_2) : \zeta_1 = \delta \quad \text{and} \quad 0 \leq \zeta_2 \leq l_\Sigma\}. \tag{3.5}$$

Let s_i be the scale factors defined by $s_i = \left|\dfrac{\partial \boldsymbol{x}}{\partial \zeta_i}\right|$, with $i = 1, 2$. Then, using the system of coordinates (ζ_1, ζ_2), the Helmholtz equation (2.1a) can be written in the layer Ω_{pml} as

$$k^2 u + \frac{1}{s_1 s_2}\left[\frac{\partial}{\partial \zeta_1}\left(\frac{s_2}{s_1}\frac{\partial u}{\partial \zeta_1}\right) + \frac{\partial}{\partial \zeta_2}\left(\frac{s_1}{s_2}\frac{\partial u}{\partial \zeta_2}\right)\right] = 0. \tag{3.6}$$

Taking into account the formulas given by (3.1), the scale factors s_1 and s_2 become

$$s_1 = 1 \quad \text{and} \quad s_2 = 1 + \kappa\zeta_1. \tag{3.7}$$

For time harmonic problems, the PML system is usually derived by complex stretching the normal coordinate that corresponds to the direction where waves are damped in the fictitious layer:

$$\zeta_1 \longrightarrow \hat{\zeta}_1(\zeta_1) = \zeta_1 + \frac{\mathrm{i}}{\omega}\int_0^{\zeta_1} \sigma(s)\mathrm{d}s, \quad \text{with} \quad \zeta_1 \in [0, \delta]. \tag{3.8}$$

Here, the frequency ω is related to the wavenumber k and the propagation speed c of the medium by $\omega = ck$, σ is the absorption function and δ is the layer thickness. These yield the complex stretching map

$$\hat{\boldsymbol{x}}(\zeta_1, \zeta_2) = \hat{\zeta}_1 \boldsymbol{n}(\zeta_2) + \boldsymbol{p}(\zeta_2) \tag{3.9}$$

and the new scale factors

$$\hat{s}_1 = 1 + \frac{\mathrm{i}\sigma}{\omega} \quad \text{and} \quad \hat{s}_2 = 1 + \kappa\hat{\zeta}_1. \tag{3.10}$$

The function σ is chosen such that

$$\sigma(\zeta_1) = 0 \text{ for } \zeta_1 \leq 0, \sigma(\zeta_1) > 0 \text{ for } \zeta_1 > 0, \text{ and } \lim_{\zeta_1 \longrightarrow +\infty}\int_0^{\zeta_1} \sigma(s)\mathrm{d}s = +\infty. \tag{3.11}$$

Under the analytic continuation $\boldsymbol{x} \longrightarrow \hat{\boldsymbol{x}}$, Equation (3.6) becomes

$$k^2 u + \frac{1}{\hat{s}_1 \hat{s}_2}\left[\frac{\partial}{\partial \zeta_1}\left(\frac{\hat{s}_2}{\hat{s}_1}\frac{\partial u}{\partial \zeta_1}\right) + \frac{\partial}{\partial \zeta_2}\left(\frac{\hat{s}_1}{\hat{s}_2}\frac{\partial u}{\partial \zeta_2}\right)\right] = 0. \tag{3.12}$$

Let us set

$$\hat{\sigma} = \frac{1}{\zeta_1 + \frac{1}{\kappa}}\int_0^{\zeta_1} \sigma(s)\mathrm{d}s, \quad \gamma = 1 + \frac{\mathrm{i}\sigma}{\omega} \quad \text{and} \quad \hat{\gamma} = 1 + \frac{\mathrm{i}\hat{\sigma}}{\omega}. \tag{3.13}$$

Then we have

$$\hat{s}_2 = (1 + \kappa\zeta_1)\hat{\gamma}. \tag{3.14}$$

From the view point of implementation in the FEM, it is practical to transform Equation (3.12) back to the Cartesian coordinates system to obtain

$$-ak^2 u - \boldsymbol{\nabla}\cdot(\boldsymbol{A}\boldsymbol{\nabla}u) = 0, \tag{3.15}$$

where $a = \gamma\hat{\gamma}$, $\boldsymbol{A} = \dfrac{\hat{\gamma}}{\gamma}\boldsymbol{n}\otimes\boldsymbol{n} + \dfrac{\gamma}{\hat{\gamma}}\boldsymbol{t}\otimes\boldsymbol{t}$ (see Appendix A), and the notation '$\otimes$' refers to the tensor product of two vectors. Let us point out that for $\zeta_1 \leq 0$, we have $a = 1$ and $\boldsymbol{A} = \boldsymbol{I}$ (the identity matrix). Following [36, 37], a simple absorbing boundary condition, suitable for an evanescent Hankel function, is imposed on the outer boundary Σ_δ:

$$(\boldsymbol{A}\boldsymbol{\nabla}u)\cdot\boldsymbol{n} - \mathrm{i}\hat{\gamma}ku \quad = \quad 0, \quad \text{on} \quad \Sigma_\delta. \tag{3.16}$$

By setting $\hat{\Omega} = \Omega \cup \Omega_{\text{pml}}$, the PML problem associated with (2.1) can be written in the Cartesian coordinates as

$$\begin{cases} -ak^2 u - \boldsymbol{\nabla}\cdot(\boldsymbol{A}\boldsymbol{\nabla}u) = 0, & \text{in} \quad \hat{\Omega} & \text{(3.17a)} \\ \boldsymbol{\nabla}u\cdot\boldsymbol{n} = g, & \text{on} \quad \Gamma_D & \text{(3.17b)} \\ (\boldsymbol{A}\boldsymbol{\nabla}u)\cdot\boldsymbol{n} = \mathrm{i}\hat{\gamma}ku, & \text{on} \quad \Sigma_\delta. & \text{(3.17c)} \end{cases}$$

One of the parameters that affect the performance of the PML is the absorption function σ. Here a standard parabolic profile is assumed:

$$\sigma(\zeta_1) = \sigma_0\left(\frac{\zeta_1}{\delta}\right)^2, \ 0 \leq \zeta_1 \leq \delta, \quad \text{with} \quad \sigma_0 = \frac{3}{2\delta}\mathrm{Log}\left(\frac{1}{R_0}\right), \tag{3.18}$$

where R_0 is the modulus of the reflection coefficient at normal incidence [37]. Typical choices are $R_0 = 10^{-1}, 10^{-2}, \cdots$. Due to numerical dispersion which has an influence on the discrete PML behaviour, it was pointed out in [37, 66] that, at a fixed mesh grid resolution in the artificial layer, largest value of σ_0 does not yield necessarily the smallest reflection. A remedy to this drawback is the use of a singular absorbing function [39, 40], or *hp* adaptation [67]. The difficulty relying on tuning the parameter σ_0 seems likely to hold for low order FEM. This can be seen through the numerical study carried out in this work, where the absorption function defined by (3.18) and high order BBFEM are used. Indeed, choosing R_0 small enough, helps significantly in reducing reflection.

For comparison purposes against the radial shaped PML (rPML), the second order BGT_2 [13] given by

$$(\mathrm{rBGT}_2) \qquad \frac{\partial u}{\partial r} = \left(ik - \frac{1}{2\rho} + \frac{1}{8\rho^2(\frac{1}{\rho} - ik)}\right)u + \frac{1}{2\rho^2(\frac{1}{\rho} - ik)}\frac{\partial^2 u}{\partial\theta^2}, \quad \text{on} \quad \Sigma, \tag{3.19}$$

is considered as well, where the artificial boundary Σ is a circle defined by

$$\Sigma \quad = \quad \{\boldsymbol{x} = (x_1, x_2) \in \mathbb{R}^2 : x_1^2 + x_2^2 = \rho^2\}. \tag{3.20}$$

Additionally, an elliptical shaped PML (ePML) is used and compared against the symmetrical BGT_2 [68]:

(eBGT_2)
$$\boldsymbol{\nabla} u \cdot \boldsymbol{n} = \left(ik - \frac{\kappa}{2} + \frac{\kappa^2}{8(\kappa - ik)} \right) u + \frac{\partial}{\partial \zeta_2} \left(\frac{1}{2(\kappa - ik)} \frac{\partial u}{\partial \zeta_2} \right), \quad \text{on} \quad \Sigma, \tag{3.21}$$

which applies for more general convex shapes. Here Σ is an ellipse given by

$$\Sigma \quad = \quad \{\boldsymbol{x} = (x_1, x_2) \in \mathbb{R}^2 : \frac{x_1^2}{\rho_1^2} + \frac{x_2^2}{\rho_2^2} = 1\}, \tag{3.22}$$

where ρ_1 and ρ_2 are the semi-major and semi-minor axes, respectively. There are other approaches to derive ABCs like BGT_2 when the artificial boundary Σ is an ellipse; see for instance references [69–72].

Let us denote by $\mathcal{B}$ the ABC operator involved in (3.19) or (3.21). Then the BGT_2 problem associated with (2.1) is given by

$$\begin{cases} -k^2 u - \Delta u = 0, & \text{in} \quad \Omega & \text{(3.23a)} \\ \boldsymbol{\nabla} u \cdot \boldsymbol{n} = g, & \text{on} \quad \Gamma_D & \text{(3.23b)} \\ \boldsymbol{\nabla} u \cdot \boldsymbol{n} = \mathcal{B} u, & \text{on} \quad \Sigma. & \text{(3.23c)} \end{cases}$$

Practical wave scattering problems may involve scatterers with curved boundaries. Moreover, to efficiently model the PML in curvilinear coordinates, accurate boundary representation is needed. The next Section is devoted to the blending map method used in this work.

4 Boundary representation

In p-FEM, it is practical to work with a relatively coarse mesh, containing large elements compared to the wavelength, and increase the polynomial order to efficiently resolve the wave at a high wavenumber. However, when the mesh grid contains elements with curved edges, low order polynomial interpolation of the geometry may induce a significant error. Therefore, an accurate geometric description is crucial for such problems.

Let us consider a partition of the domain Ω into a set of non-overlapping finite elements T_e. Let $\hat{T}$ be the reference element defined by

$$\hat{T} = \{\boldsymbol{\xi} = (\xi_1, \xi_2) : \quad 0 \leq \xi_1 \leq 1, \quad 0 \leq \xi_2 \leq 1 - \xi_1\}. \tag{4.1}$$

Let $\boldsymbol{q}_i$ and $\boldsymbol{q}_{ij}$ be the nodal points of T_e (see Figure 3). The barycentric coordinates relative to the reference element $\hat{T}$ are given by

$$\lambda_1(\boldsymbol{\xi}) = \xi_1, \quad \lambda_2(\boldsymbol{\xi}) = \xi_2 \quad \text{and} \quad \lambda_3(\boldsymbol{\xi}) = 1 - \xi_1 - \xi_2. \tag{4.2}$$

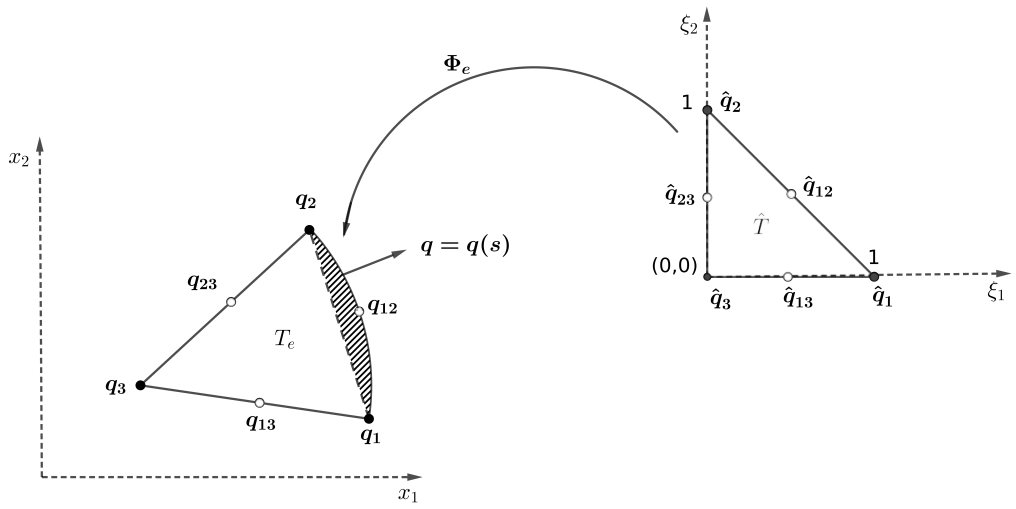

Figure 3: Reference map for a curved triangular element.

In this work the linear blending map due to Gordon and Hall [58, 59] is adopted. To illustrate this method, let consider the case of a triangular element with only one curved edge and assume it is edge $e_1 = (\boldsymbol{q}_1\boldsymbol{q}_2)$ (see Figure 3), given by its parametric form $\boldsymbol{q} = \boldsymbol{q}(s)$, where $0 \leq s \leq 1$, $\boldsymbol{q}(0) = \boldsymbol{q}_1$ and $\boldsymbol{q}(1) = \boldsymbol{q}_2$. Following [60], a map denoted Φ_e and defined from $\hat{T}$ to T_e can be written as

$$\Phi_e(\boldsymbol{\xi}) = \lambda_1(\boldsymbol{\xi})\boldsymbol{q}_1 + \lambda_2(\boldsymbol{\xi})\boldsymbol{q}_2 + \lambda_3(\boldsymbol{\xi})\boldsymbol{q}_3 + \frac{\lambda_1(\boldsymbol{\xi})\lambda_2(\boldsymbol{\xi})}{\xi_2(1-\xi_2)}\left[\boldsymbol{q}(\xi_2) - ((1-\xi_2)\boldsymbol{q}_1 + \xi_2\boldsymbol{q}_2)\right]. \tag{4.3}$$

For instance, if edge e_1 is the circular arc defined by the parametric form $\boldsymbol{q} = \rho(\cos\theta, \sin\theta)$, with $\theta \in [\theta_1, \theta_2]$, then

$$\boldsymbol{q}(s) = \rho(\cos((1-s)\theta_1 + s\theta_2), \sin((1-s)\theta_1 + s\theta_2))^\top, \quad \text{with} \quad s \in [0,1]. \tag{4.4}$$

This method applies for triangular elements where two or all sides are curved as well. Let us point out that the function

$$\boldsymbol{g} : \xi_2 \longmapsto \frac{\boldsymbol{q}(\xi_2) - ((1-\xi_2)\boldsymbol{q}_1 + \xi_2\boldsymbol{q}_2)}{\xi_2(1-\xi_2)}$$

can be continuously extended to the whole interval $[0,1]$ by taking

$$\boldsymbol{g}(0) = \boldsymbol{q}'(0) + \boldsymbol{q}_2 - \boldsymbol{q}_1 \quad \text{and} \quad \boldsymbol{g}(1) = -\boldsymbol{q}'(1) + \boldsymbol{q}_2 - \boldsymbol{q}_1, \tag{4.5}$$

where the prime ''' refers to differentiation with respect to the argument. It suffices to see that

$$\boldsymbol{g}(\xi_2) = \frac{\boldsymbol{q}(\xi_2) - \boldsymbol{q}_1}{\xi_2} - \frac{\boldsymbol{q}(\xi_2) - \boldsymbol{q}_2}{\xi_2 - 1}. \tag{4.6}$$

Additionally, the following six-node Lagrange interpolation map

$$\Phi_e(\boldsymbol{\xi}) \quad = \quad \sum_i \lambda_i(\boldsymbol{\xi})(2\lambda_i(\boldsymbol{\xi}) - 1)\boldsymbol{q}_i + 4\sum_{i<j} \lambda_i(\boldsymbol{\xi})\lambda_j(\boldsymbol{\xi})\boldsymbol{q}_{ij} \tag{4.7}$$

is used and compared against the blending map method.

5 Bernstein-Bézier FE discretisation

Under the previous notations, the approximate solution, denoted by u_h, by Bernstein-Bézier FE of either Problem (3.17) or (3.23), can be written element-wise in the form

$$u_h(\boldsymbol{x}) = \sum_{|\boldsymbol{\alpha}|=p} u_{\boldsymbol{\alpha}} B^p_{\boldsymbol{\alpha}}(\boldsymbol{\xi}), \tag{5.1}$$

where $B^p_{\boldsymbol{\alpha}}$ are the Bernstein polynomials of degree $p \in \mathbb{Z}_+$, associated with the reference element $\hat{T}$ and given by

$$B^p_{\boldsymbol{\alpha}}(\boldsymbol{\xi}) = \begin{pmatrix} p \\ \boldsymbol{\alpha} \end{pmatrix} \boldsymbol{\lambda}^{\boldsymbol{\alpha}}(\boldsymbol{\xi}). \tag{5.2}$$

The order $|\boldsymbol{\alpha}|$ of a multi-index $\boldsymbol{\alpha} = (\alpha_1, \alpha_2, \alpha_3)$ in $\mathbb{Z}^3_+$ is defined by $|\boldsymbol{\alpha}| = \sum_{i=1,3} \alpha_i$, $\boldsymbol{\lambda}^{\alpha} = \lambda_1^{\alpha_1}\lambda_2^{\alpha_2}\lambda_3^{\alpha_3}$ and

$$\begin{pmatrix} p \\ \boldsymbol{\alpha} \end{pmatrix} = \frac{p!}{\alpha_1!\alpha_2!\alpha_3!}. \tag{5.3}$$

Multiplying by a test function $\bar{v}$ (the complex conjugate of $v \in H^1(\hat{\Omega})$) in the PML problem (3.17) and integrating by parts over $\hat{\Omega}$, we obtain the weak form

$$-ak^2 \int_{\hat{\Omega}} u\bar{v}\, \mathrm{d}\hat{\Omega} + \int_{\hat{\Omega}} \boldsymbol{A}\boldsymbol{\nabla} u \cdot \boldsymbol{\nabla}\bar{v}\, \mathrm{d}\hat{\Omega} + \mathrm{i}k \int_{\Sigma_\delta} \hat{\gamma} u\bar{v}\, \mathrm{d}\Sigma = \int_{\Gamma_D} g\bar{v}\, \mathrm{d}\Gamma, \quad \forall v \in H^1(\hat{\Omega}). \tag{5.4}$$

Similarly, the BGT_2 problem (3.23) yields

$$-k^2 \int_{\Omega} u\bar{v}\, \mathrm{d}\Omega + \int_{\Omega} \boldsymbol{\nabla} u \cdot \boldsymbol{\nabla}\bar{v}\, \mathrm{d}\Omega + \int_{\Sigma} \mathcal{B} u\bar{v}\, \mathrm{d}\Sigma = \int_{\Gamma_D} g\bar{v}\, \mathrm{d}\Gamma, \quad \forall v \in H^1(\Omega). \tag{5.5}$$

To ensure C^0 conformity of BBFEM, the matching of edge modes of a similar shape is required. This is performed based on a global orientation of the FE edges (see [73, 74] for further details).

The element integrals arising in the discrete weak forms of the variational problems (5.4) and (5.5) are evaluated using a high order Gauss-Legendre integration scheme. Here, an element without any edge in contact with curved boundaries is interpolated using a standard linear FE map and hence analytical integration rules can be used. However, for curved elements that are accurately represented based on the blending map of Gordon and Hall, numerical integration is performed.

The resulting linear system from the approximation by BBFEM of the weak forms (3.17) and (3.23) involves sparse symmetric complex valued matrices. It is solved, using a coordinate storage format, based on the multi-frontal sparse direct solver MUMPS [75].

6 Numerical results

Both rPML and ePML are validated by means of two dimensional benchmarks, based on BBFEM with static condensation [53]. This technique is very efficient in reducing the total number of DoF and bandwidth of high order FE global matrices. It consists of removing interior mode DoF from the resulting discrete algebraic system during the assembling process. Once the solution related to element boundary modes is obtained, that corresponding to interior modes is recovered by solving small linear algebraic systems at an elemental level. In all that follows, the propagation speed c of the medium is assumed to be unity, so the wavenumber is $k = \omega$. For affine elements, a rule of $p+1$ integration points is used for the evaluation of element matrices by the Gauss-Legendre integration

scheme, which is exact if the integrand is a polynomial of degree no higher than $2p+1$ [73]. The choice of the number of quadrature points with the presence of curved elements is mainly dictated by the target accuracy (see, e.g., References [77, 78] for further discussion). Since, convergence analysis is dealt with and a high level of accuracy is desired, a rule of $2p+1$ quadrature points is adopted to accommodate the variation of the Jacobian. For element right side integrals, it is required to account for the number of wavelengths per edge as well, as the integrand involves a highly oscillatory incident plane wave.

First, a benchmark test dealing with the radiation of a Hankel source is carried out to assess the performance of the blending map method of Gordon and Hall. Then, a single wave scattering problem is considered to study the h and p convergence of BBFEM combined to rPML. This domain truncation method is also compared against rBGT_2. Lastly, a multiple scattering benchmark test is considered, in which both rPML and ePML are used and compared against rBGT_2 and eBGT_2, respectively. The effect of the discrete PML parameters on accuracy is also examined.

6.1 Description of the Benchmarks

For the first two benchmarks the computation domains have an annular shape (see Figure 4). The inner and outer radii of the rBGT_2 domain Ω are a and ρ, and those of the rPML domain $\hat{\Omega}$ are a and $\rho+\delta$, respectively, where δ is the PML thickness. Both rBGT_2 and PML artificial boundaries Σ are placed at the same distance ρ from the origin.

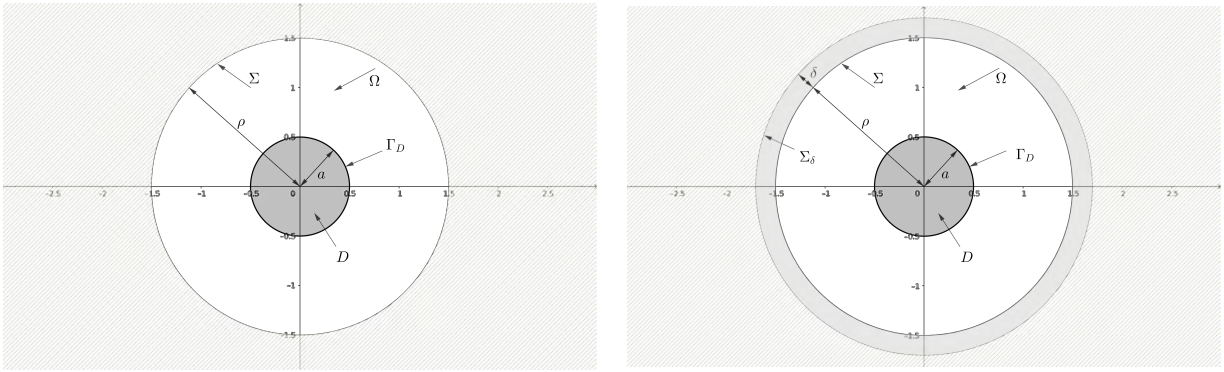

Figure 4: Computational domain for the first two benchmarks: (left) rBGT_2 domain; (right) rPML domain.

The benchmark dealing with Hankel source radiation has an analytical solution given by

$$u = \mathrm{H}_0(k|\boldsymbol{x}|), \tag{6.1}$$

where H_0 is the Hankel function of the first kind. On the boundary Γ_D, the analytical solution is enforced by taking $g = k\mathrm{H}_0'(k|\boldsymbol{x}|)$. Since rBGT_2 performs very well for harmonics of lower modes, it is chosen as a mesh truncation procedure to assess the performance of the blending map method. But the use of rPML leads to similar results, provided an adequate choice of the PML parameters R_0 and δ is made.

The second benchmark concerns the scattering of a horizontal plane wave $u_{\mathrm{in}} = \exp(\mathrm{i}kx_1)$ by a rigid circular cylinder of radius a, centered at the origin. This problem has an analytical solution given by [76]

$$u = -\sum_{m=-\infty}^{\infty} \mathrm{i}^m Z_m \mathrm{H}_m(kr)\exp(\mathrm{i}m\theta), \tag{6.2}$$

where (r, θ) denotes the polar coordinates system, J_m and H_m are respectively the Bessel and Hankel functions of the first kind and order m, and $Z_m = \dfrac{\mathrm{J}'_m(ka)}{\mathrm{H}'_m(ka)}$. At the implementation level, the above infinite expansion must be truncated to a finite number of terms $2M+1$. This generates another source of error in addition to those of discretisation and mesh truncation. In reference [79], it was shown that a sufficient condition to ensure uniqueness of the solution for the truncated Dirichlet-to-Neumann (DtN) formulation of the Helmholtz problem is $M > k\rho$. In this work, the number M is chosen such that $M \simeq 2ka$.

The last benchmark deals with a multiple scattering problem, in which an incident plane wave $u_{\text{in}} = \exp(\mathrm{i}k\boldsymbol{x} \cdot \boldsymbol{d})$ impinges upon an array of N rigid cylinders, such that $\boldsymbol{d} = (\cos\beta, \sin\beta)$ and $\beta = \pi/4$. In a such case, the diffracted waves from these separated rigid obstacles are not purely outgoing, as they may undergo multiple reflections between the scatterers.

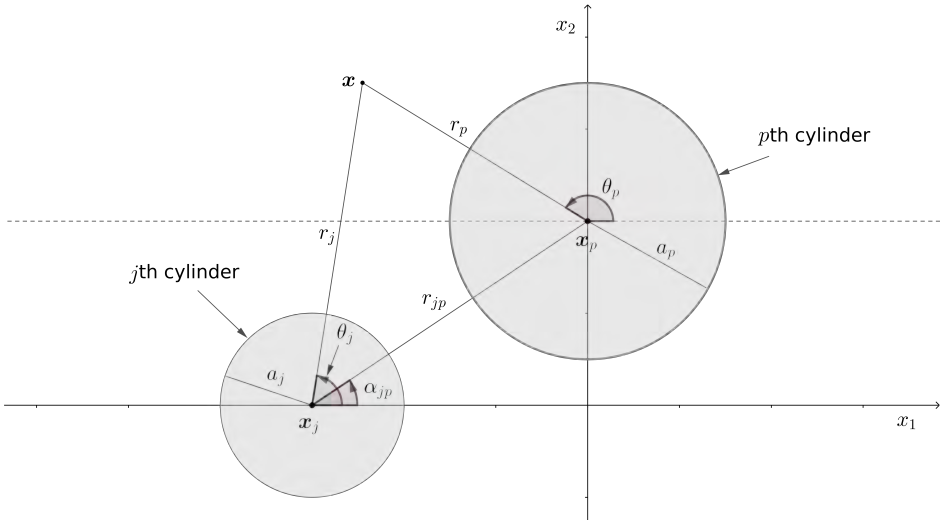

Figure 5: Schematic diagram defining the parameters of the multiple scattering problem.

An approximate analytical solution of this problem is given by [76]

$$u = \sum_{j=1}^{N} \sum_{m=-M_j}^{M_j} A_m^j Z_m^j \mathrm{H}_m(kr_j) \exp(\mathrm{i}m\theta_j), \tag{6.3}$$

where $Z_m^j = \dfrac{\mathrm{J}'_m(ka_j)}{\mathrm{H}'_m(ka_j)}$ and the unknowns $\{A_m^j\}$ are solution of the following linear system

$$\begin{aligned} A_n^p + \sum_{\substack{j=1 \\ j \neq p}}^{N} \sum_{m=-M_j}^{M_j} A_m^j Z_m^j \exp(\mathrm{i}(m-n)\alpha_{jp}) \mathrm{H}_{m-n}(kr_{jp}) &= -I_p \exp(\mathrm{i}n(\pi/2-\beta)), \\ p = 1, \cdots, N \quad \text{and} \quad n = -M_j, \cdots, M_j, & \end{aligned} \tag{6.4}$$

where $I_p = \exp(\mathrm{i}k\boldsymbol{x}_p \cdot \boldsymbol{d})$. The definitions of the parameters α_{jp} and r_{jp} are given in Figure 5.

In this benchmark, an array of five equidistant rigid cylinders of equal radii a, arranged on the x_1 axis are considered (see Figure 6). Hence $a_j = a$ and the numbers M_j can be chosen equal, i.e. $M_j = M$. The positions of the scatterers are given by $\boldsymbol{x}_i = (3(i-3)a, 0)^\top$, with $i = 1, \cdots, 5$. The

computational domains used for rBGT$_2$ and eBGT$_2$ can be deduced from Figure 6 by removing the layer Ω_{pml}. A similar benchmark is dealt with numerically using rBGT$_2$ combined to the partition of unity FE method in [80]. As can be seen from this configuration of the scatterers, the use of rBGT$_2$ or rPML leads to a large computational domain. An alternative approach to eBGT$_2$ or ePML adopted here, is to enclose each scatterer by a separate artificial boundary, as done in References [81, 82] within the DtN map and PML, respectively. It is worth noticing that the curve Σ_δ parallel to the ellipse Σ (see Figure 6 (bottom)) is not itself an ellipse. More precisely, Σ_δ is described by the parametric form

$$\boldsymbol{p} = \left(\left(\rho_1 + \frac{\delta\rho_2}{\sqrt{\rho_1^2 \sin^2\theta + \rho_2^2 \cos^2\theta}} \right) \cos\theta, \left(\rho_2 + \frac{\delta\rho_1}{\sqrt{\rho_1^2 \sin^2\theta + \rho_2^2 \cos^2\theta}} \right) \sin\theta \right)^\top, \tag{6.5}$$

where $\theta \in [0, 2\pi]$. The curvature of Σ is given by

$$\kappa = \frac{\rho_1\rho_2}{\sqrt{\rho_1^2 \sin^2\theta + \rho_2^2 \cos^2\theta}^3}. \tag{6.6}$$

The orthogonal projection of a point $\boldsymbol{x}$ in the artificial layer onto the ellipse Σ is computed numerically using Newton's Method. In order to create a FE partition of the ePML domain using a mesh generator, the outer artificial boundary Σ_δ is represented by B-splines via `CAD` and imported as a '`step`' file to `Gmsh` [83]. Further details about the derivation of rPML and ePML are given in Appendix A.

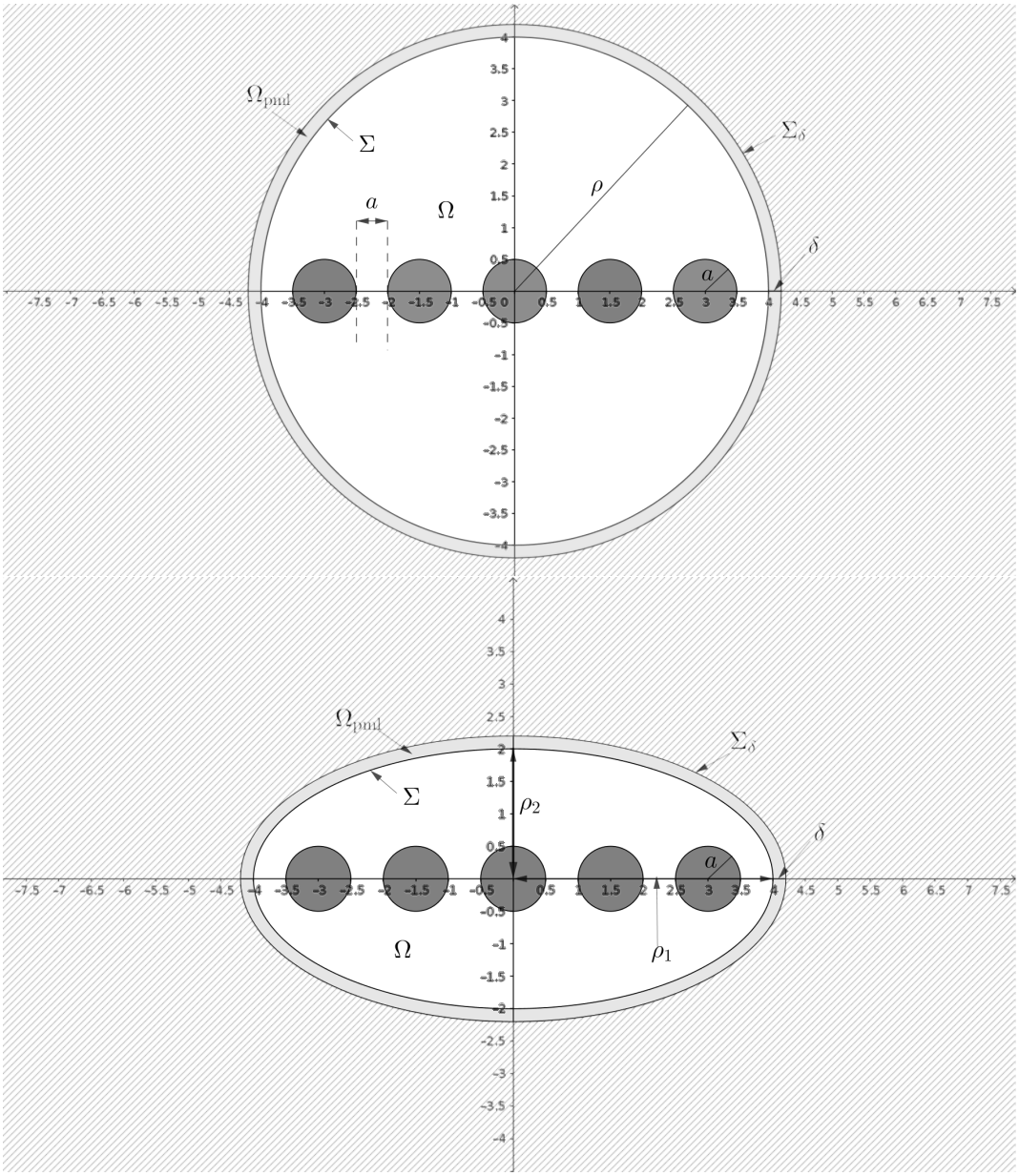

Figure 6: Computational domains for multiple scattering problem: (top) rPML domain; (bottom) ePML domain.

These benchmarks make use of a number of parameters such as the wavenumber k, the mesh size h, the polynomial order p, the PML thickness δ and the absorption coefficient R_0. The wave resolution is given by

$$\tau_\lambda = \lambda \sqrt{\frac{n_{\text{dof}}}{|\Omega|}}, \tag{6.7}$$

where $|\Omega|$ is the surface area of Ω and n_{dof} is the total number of DoF. The indicator τ_λ gives the number of DoF per wavelength λ. The accuracy of the numerical solution is measured by the following relative L^2 error

$$\epsilon_2 = \frac{\|u_h - u\|_0}{\|u\|_0} \times 100\%, \tag{6.8}$$

where $\|\cdot\|_0$ is the usual norm of $L^2(\Omega)$. For the PML numerical solution, the quantities τ_λ and ϵ_2 are evaluated using the extended and physical domains $\hat{\Omega}$ and Ω, respectively.

6.2 Hankel source radiation

In order to study the performance of the blending map method of Gordon and Hall, the sound source radiation problem is numerically solved using BBFEM combined with rBGT$_2$. This boundary representation method is compared against the six-node Lagrange interpolation map given by (4.7). The numerical experiments are performed on a sequence of eight gradually refined mesh grids (see Figure 7), where the radius ρ of the outer circle Σ is chosen such that $\rho = 3a$. Since the analytical solution is enforced on Γ_D as mentioned previously, the only sources of error are those of the BBFEM discretisation and rBGT$_2$ mesh truncation.

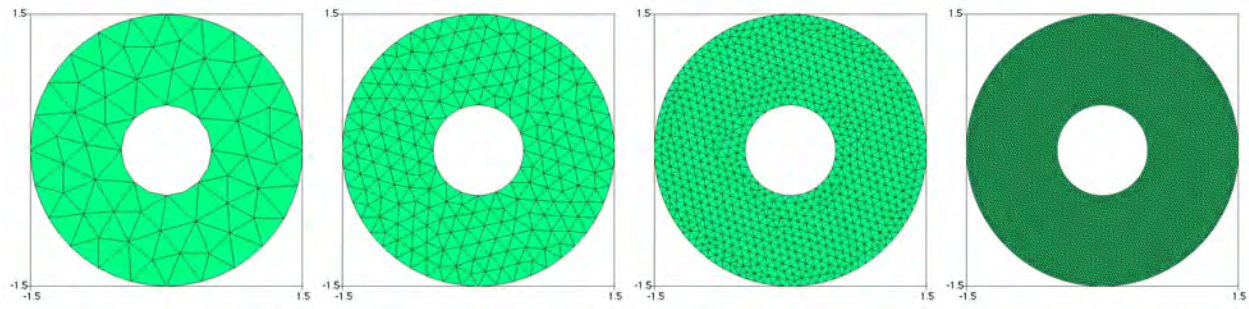

Figure 7: Typical unstructured mesh grids used for rBGT$_2$; from the left to the right: M_1 ($h = 0.88a$), $M_{1/2}$ ($h = 0.5a$), $M_{1/4}$ ($h = 0.28a$) and M_f ($h = 0.08a$).

First, h-convergence analysis is carried out. In Figure 8, the relative L_2 error ϵ_2 is plotted against the number τ_λ of DoF per wavelength, for both Lagrange interpolation and blending map methods at wavenumbers $ka = 5\pi$ and $ka = 10\pi$, where the polynomial order p is set equal to 6.

Unless an accurate solution is sought, the results in Figure 8 indicate that the Lagrange interpolation and blending map methods have a similar performance. However, the L^2 error with the Lagrange map stagnates as τ_λ increases. This is not surprising, because low order polynomial interpolation maps of the geometry are inconsistent with high order FEM. Due to round off error which is very significant with ill conditioning, the L^2 error with the blending map method becomes saturated for higher wave resolutions (see Figure 8(a)). But as can be seen, this method enables the recovery of an asymptotically algebraic decay of the L^2 error which scales as τ_λ^{-p-1}.

Next, p-convergence analysis is investigated, where numerical experiments are performed on mesh grid $M_{1/2}$ (see Figure 7), for the same two wavenumbers as before. Let us notice that at the

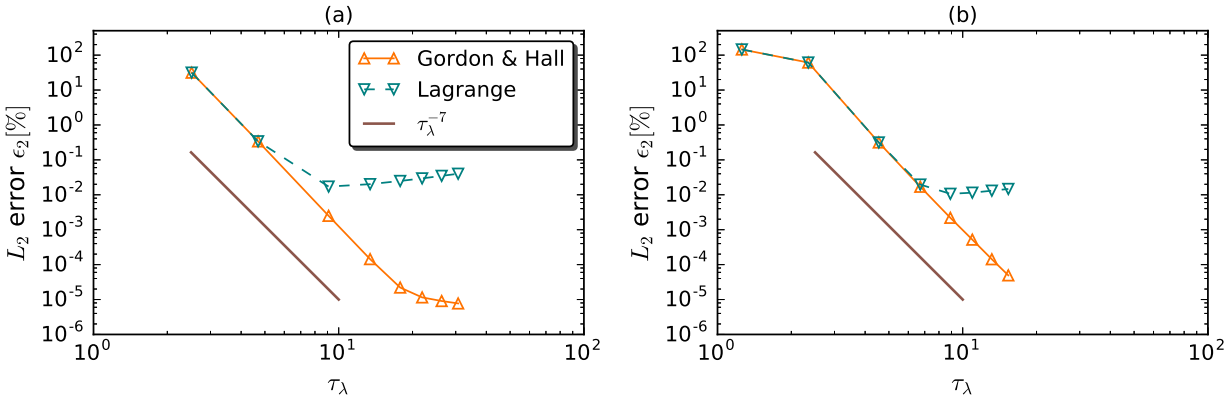

Figure 8: The L^2 error versus τ_λ, h-refinement with $p = 6$: (a) $ka = 5\pi$; $ka = 10\pi$.

wavenumber $ka = 10\pi$, elements of the mesh grid $M_{1/2}$ may contain up to $h/\lambda \simeq 2.5$ wavelengths. Figure 9 shows the L_2 error ϵ_2 versus the polynomial order p, at the wavenumbers $ka = 5\pi$ and $ka = 10\pi$. It is observed from these results that the Lagrange interpolation and blending maps lead to a similar accuracy for moderate approximation orders: $p \leq 7$ for $ka = 5\pi$ (Figure 9(a)), and $p \leq 8$ for $ka = 10\pi$ (Figure 9(b)). As before, it can be seen that the L_2 error with the Lagrange interpolation map stagnates, but now with the increase of the polynomial order p. Most notably, results of Figure 9 show clearly an exponential decay of the L^2 error as the approximation order p increases.

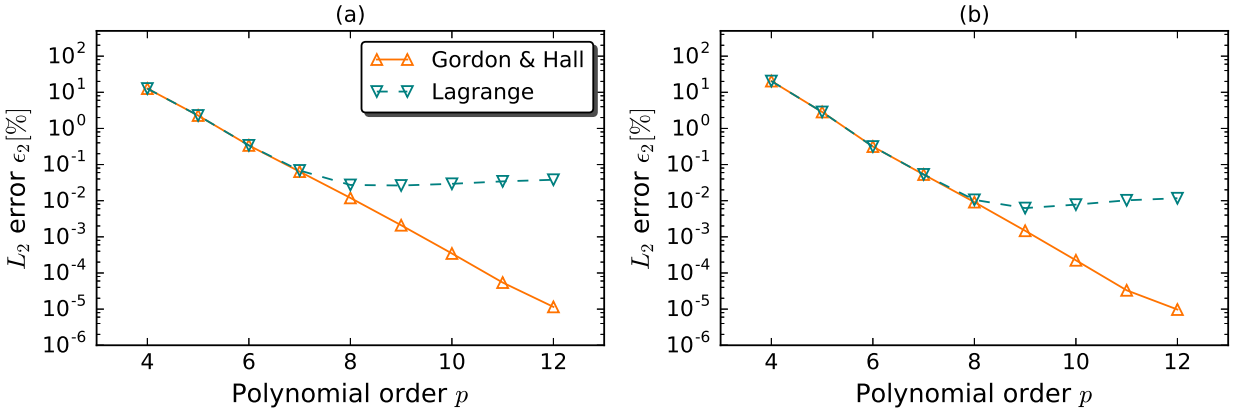

Figure 9: The L^2 error versus the polynomial order, p-refinement with $h = 0.50a$: (a) $ka = 5\pi$; (b) $ka = 10\pi$.

For similar studies, relying on nodal and modal curving methods and Non-uniform rational B-splines (NURBS) representation of the geometry, the reader is referred to references [77, 78].

6.3 Wave scattered by a rigid cylinder

This scattering problem is numerically solved, based on BBFEM using rBGT$_2$ and rPML as mesh truncation methods. Curved geometries are represented by the blending map of Gordon and Hall. The mesh grids used with rBGT$_2$ are those of the previous benchmark (see Figure 7). Numerical experiments with rPML are performed on the sequence of mesh grids depicted in Figure 10. The parameters δ and R_0 are set equal to $0.4a$ and 10^{-10}, respectively. The effect of the PML parameters

on the accuracy will be studied for both rPML and ePML in the third benchmark. In Figure 10, the parameter mesh sizes are not indicated, because mesh grids of the physical domain Ω are the same as those of Figure (7) used with rBGT$_2$, and the L^2 error with rPML is evaluated on Ω.

Since the analytical solution of this benchmark is defined by a truncated expansion, an additional source of error due to truncation should be taken into account. This suggests that we investigate first the effect of cylindrical waves of higher modes m, on the L^2 error. These harmonics involved in the infinite expansion (6.2) are given by $u_m = Z_m \mathrm{H}_m(kr)\exp(\mathrm{i}m\theta)$. As for the first benchmark, these analytical solutions are enforced on Γ_D, by taking $g = kZ_m \mathrm{H}'_m(kr)\exp(\mathrm{i}m\theta)$.

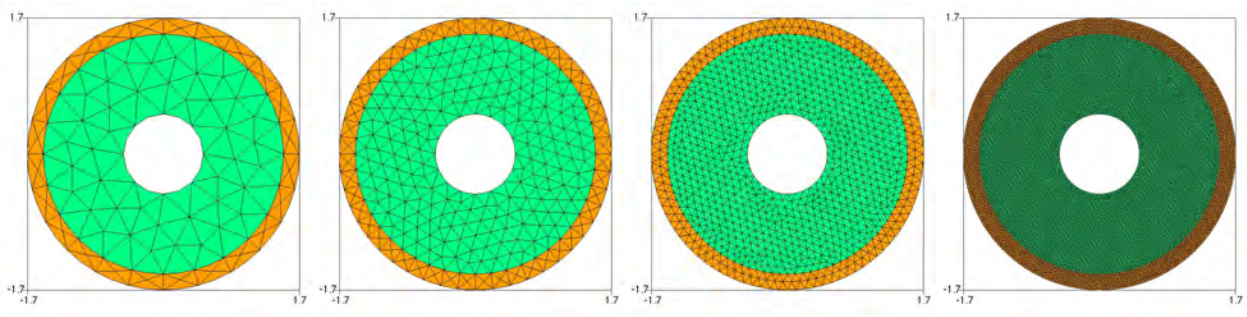

Figure 10: Typical unstructured mesh grids used for the single scattering problem with rPML; from the left to the right: $\hat{M}_1$, $\hat{M}_{1/2}$, $\hat{M}_{1/4}$ and $\hat{M}_f$.

6.3.1 Effect of harmonics of higher modes on accuracy

A study in this context at the continuous level comparing the reflection coefficients of rBGT$_2$ and rPML was conducted in [84]. It was concluded that by increasing the absorption coefficient, the PML outperforms BGT$_2$ for all propagating modes. Related work using rBGT$_2$ can be found in [85].

Here, numerical experiments with rBGT$_2$ are performed on mesh grids $M_{1/2}$ and $M_{1/4}$, while those with rPML are on mesh grids $\hat{M}_{1/2}$ and $\hat{M}_{1/4}$. Figure 11 shows the L_2 error ϵ_2 against the ratio m/ka, for the wavenumbers $ka = 5\pi$ and $ka = 10\pi$. The polynomial order p is set equal to 10. Using mesh grids $M_{1/2}$ and $\hat{M}_{1/2}$, the approximate solutions of the harmonics $\{u_m\}$ require the wave resolutions: $\tau_\lambda \backsimeq 6.20$ and $\tau_\lambda \backsimeq 7.45$ at the wavenumber $ka = 5\pi$, with rBGT$_2$ and rPML, respectively.

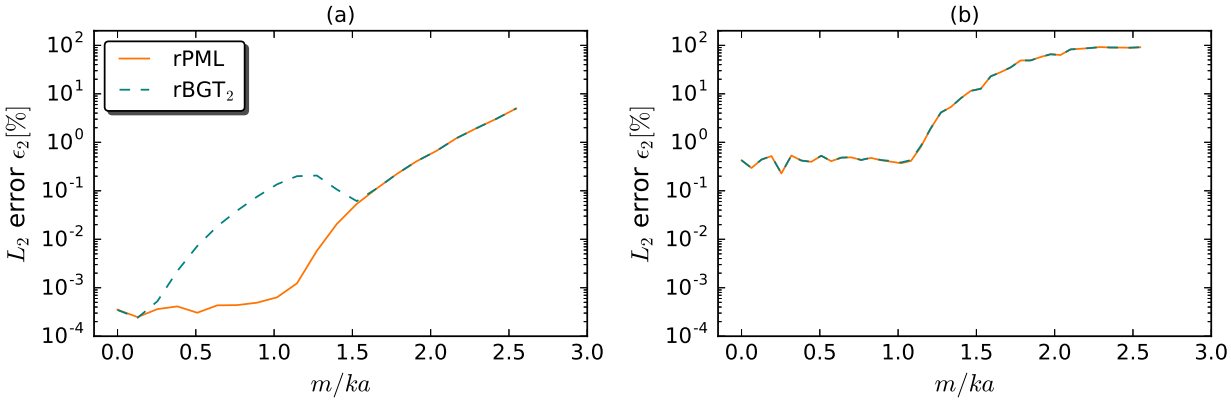

Figure 11: The L^2 error versus m/ka, with $h = 0.5a$ and $p = 10$: (a) $ka = 5\pi$ and (b) $ka = 10\pi$.

The results shown in Figure 11(a) indicate that a similar accuracy is achieved with rBGT$_2$ and rPML, for harmonics with lower modes ($m \lesssim 0.25k$). As the ratio m/ka increases, with $m \leq ka$, rBGT$_2$ performs poorly, while the error using rPML is about three orders of magnitude smaller. When $m > ka$, it is also seen that the L_2 error grows, as the ratio m/ka increases. For harmonics of higher modes ($m \gtrsim 1.5ka$), it can be observed from Figure 11(a) that both rBGT$_2$ and rPML yield a similar accuracy.

Now, by increasing the wavenumber ka to 10π, the wave resolutions to solve the harmonics u_m are only $\tau_\lambda \backsimeq 3.01$ and $\tau_\lambda \backsimeq 3.72$ with rBGT$_2$ and rPML, respectively. In such a case where the wave is not sufficiently well resolved, results of Figure 11(b) show that rBGT$_2$ and rPML perform similarly.

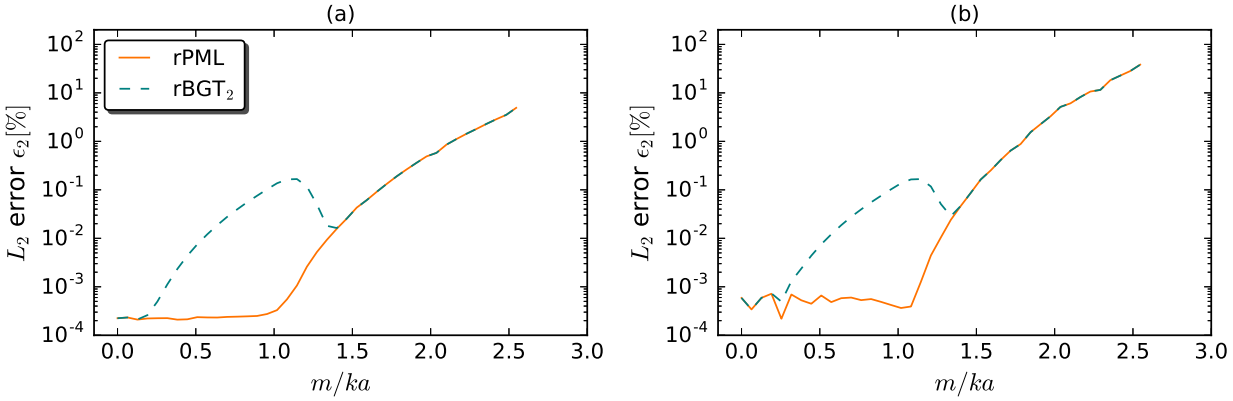

Figure 12: The L^2 error versus m/ka, for $ka = 10\pi$: (a) $h = 0.28a$ and $p = 10$; (b) $h = 0.5a$ and $p = 15$.

To confirm it is a wave resolution issue, h and p refinements are performed, by keeping the wavenumber $ka = 10\pi$. First, numerical experiments are carried out on mesh grids $M_{1/4}$ and $\hat{M}_{1/4}$, with the approximation order $p = 10$. These yield improved wave resolutions $\tau_\lambda \backsimeq 6.01$ and $\tau_\lambda \backsimeq 6.69$ with rBGT$_2$ and rPML, respectively.The results depicted in Figure 12(a) show the same trend as before (see Figure 11(a)). In a similar fashion, by keeping mesh grids $M_{1/2}$ and $\hat{M}_{1/2}$ and increasing the polynomial order to $p = 15$, the wave resolutions become: $\tau_\lambda \backsimeq 3.84$ and $\tau_\lambda \backsimeq 4.61$ with rBGT$_2$ and rPML, respectively. One can observe again in the results displayed in Figure 12(b) the same behaviour of the L^2 error with respect to the ratio m/ka as previously (see Figures 11(a) and 12(a)).

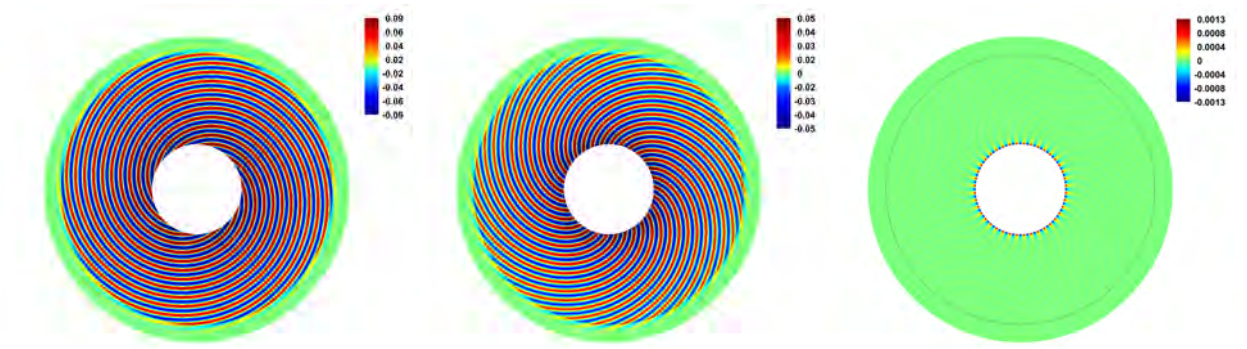

Figure 13: Real part of the rPML numerical solution computed on mesh grid $\hat{M}_{1/2}$, with $p = 10$, for the wave number $ka = 10\pi$: (left) $m = 10$ and $\epsilon_2 = 0.0002\%$; (middle) $m = 30$ and $\epsilon_2 = 0.0002\%$; (right) $m = 40$ and $\epsilon_2 = 0.005\%$.

For illustration purposes, contour plots of the real part of the rPML numerical solution are depicted in Figure 13, for the wavenumber $ka = 10\pi$, where computations are performed on mesh grid $\hat{M}_{1/2}$, with a polynomial order $p = 10$. These make use of $n_{\text{ndof}} = 28,080$ and $\tau_\lambda \simeq 6.68$ to achieve the indicated accuracies. Three kinds of waves can be seen: a propagating wave ($m < ka$), a grazing wave ($m \backsimeq ka$) and an evanescent wave ($m > ka$). Unless higher evanescent modes whose decay is much faster as $1/r^m$ (see Reference [86]) are not involved, the results shown in Figure 13 indicate that rPML enables the scheme to achieve a high level of accuracy. Similar numerical tests are dealt with in [51] to assess the performance of p-FEM.

6.3.2 Convergence analysis

In addition to the errors due to the PML truncation and FE discretization, there is another error due the truncation of the infinite expansion (6.2) to a finite number of terms $2M + 1$, because the approximate analytical solution no longer satisfies the Neumann boundary condition (3.17b). In all that follows, the number M is taken such that $M \backsimeq 2ka$.

In a similar fashion as in the first benchmark, h-convergence analysis is investigated by using rBGT$_2$ and rPML. In this scattering problem, the function g is given by $g = -\boldsymbol{\nabla} u_{\text{in}} \cdot \boldsymbol{n}$, where $u_{\text{in}} = \exp(\mathrm{i}kx_1)$. Numerical experiments with rBGT$_2$ and rPML are performed, respectively, on the sequence of mesh grids in Figures 7 and 10. As before the parameters δ and R_0 of rPML are set equal to $0.4a$ and 10^{-10} , respectively.

Figure 14 shows the relative L_2 error ϵ_2 against the number τ_λ of DoF per wavelength, for the wavenumbers $ka = 5\pi$ and $ka = 10\pi$. The polynomial order p being set equal to 6. In contrast to the case of the Hankel source benchmark, the results shown in Figure 14 indicate a poor performance of rBGT$_2$ at a high wave resolution. This is likely due to the fact that the reflection of harmonics with intermediate mode orders using rBGT$_2$ is more significant. However, at a low wave resolution, rBGT$_2$ and rPML lead to a similar accuracy. Let us notice that for the wavenumbers $ka = 5\pi$ and $ka = 10\pi$, the number of involved harmonics in the approximate analytical solution are $M \simeq 31$ and $M \simeq 62$, respectively. It is also evident from the results shown in Figure 14, that there is an algebraic decay of the L^2 error which scales asymptotically as τ_λ^{-p-1}.

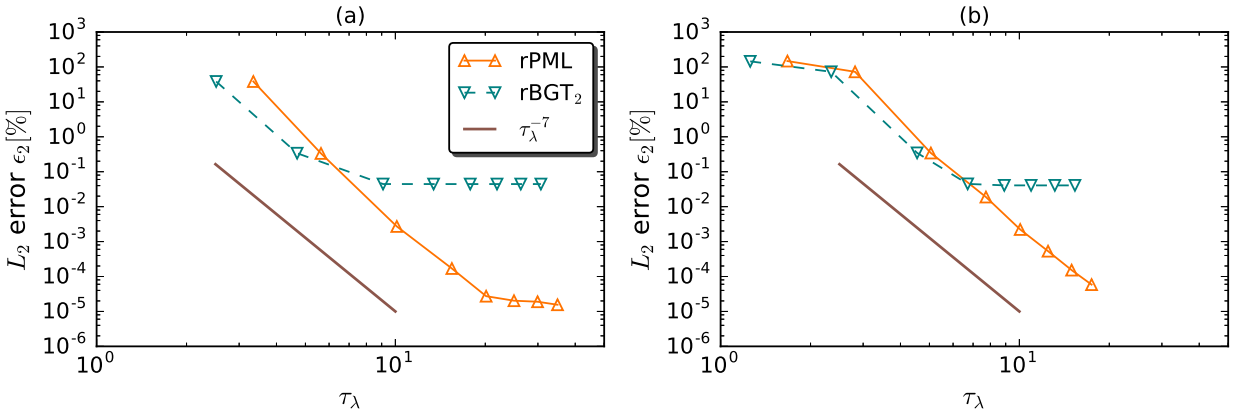

Figure 14: The L^2 error versus τ_λ; h-refinement with $p = 6$: (a) $ka = 5\pi$ and (b) $ka = 10\pi$.

Results with the wavenumber $ka = 20\pi$ and approximation order $p = 12$, are depicted in Figure 15. A similar trend as before can be seen for both rBGT$_2$ and rPML.

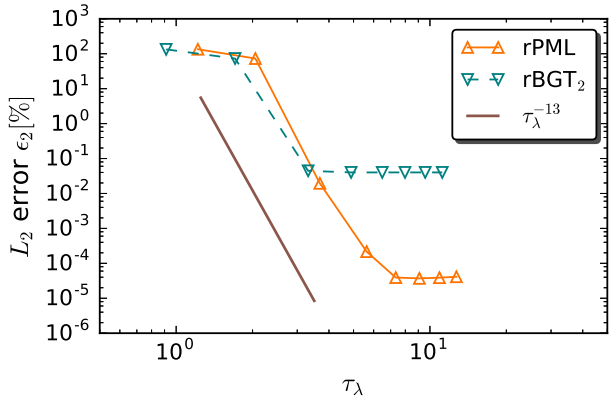

Figure 15: The L^2 error versus τ_λ; h-refinement with $p = 12$, $ka = 20\pi$.

Now, p-convergence analysis is carried out. Numerical experiments are performed on mesh grids $M_{1/2}$ and $\hat{M}_{1/2}$, with the wavenumbers $ka = 5\pi$ and $ka = 10\pi$. A test case with $ka = 20\pi$, and mesh grids $M_{1/4}$ and $\hat{M}_{1/4}$ are also considered. Let us notice that at the wavenumber $ka = 20\pi$, elements of the computational meshes $M_{1/4}$ and $\hat{M}_{1/4}$ may contain up to $h/\lambda \backsimeq 2.8$ wavelengths.

Figure 16 shows the relative L_2 error ϵ_2 against the polynomial order p, with both rBGT$_2$ and rPML. It can be seen again from results of Figure 16 that rBGT2 performs poorly at a high wave resolution. However, as before, rBGT2 and rPML lead to a similar accuracy, when the wave is not sufficiently well resolved. A trend similar to that found previously is observed, with the p-refinement.

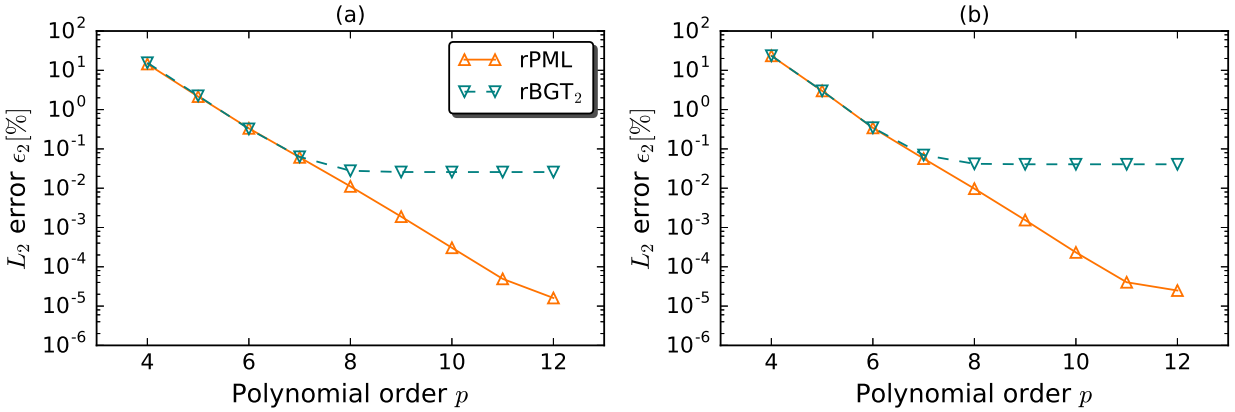

Figure 16: The L^2 error versus the polynomial order p; p-refinement with $h = 0.5a$: (a) $ka = 5\pi$ and (b) $ka = 10\pi$.

In a similar fashion, numerical experiments are performed on the mesh grids $M_{1/4}$ and $\hat{M}_{1/4}$. The wavenumber ka is now set equal to 20π. The obtained results are depicted in Figure 17 and similar trends as before can be seen.

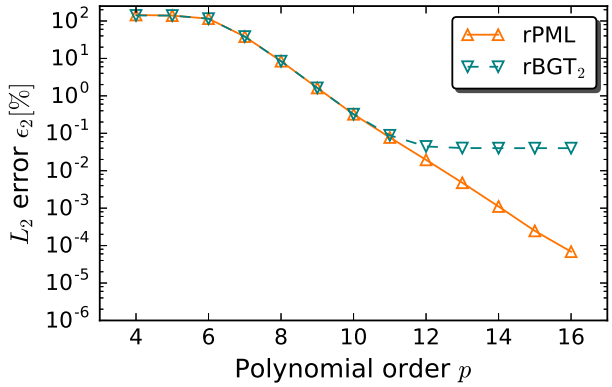

Figure 17: The L^2 error versus the polynomial order p; p-refinement with $h = 0.28a$: $ka = 20\pi$.

In summary, the overall conclusions are:

- rBGT2 and rPML have a similar performance at a low wave resolution;
- rBGT2 performs poorly when the wave is sufficiently well resolved;
- The h and p versions of BBFEM combined to rPML enable the scheme to achieve the usual algebraic and exponential convergence of high order FEMs, provided an adequate choice of the PML parameters is made to push the error induced by the PML truncation below the FE discretization error.

6.4 Multiple scattering

Numerical results are now presented for the multiple scattering benchmark. The artificial boundary Σ of rPML or rBGT$_2$ is placed at a distance $\rho = 8a$ from the origin to enclose the scatterers (see Figure 6 (top)), while the parameters ρ_1 and ρ_2 of ePML or eBGT$_2$ are taken such that $\rho_1 = \rho$ and $\rho_2 = \rho/2$ (see Figure 6 (bottom)).

6.4.1 Influence of the layer thickness δ

For both rPML and ePML, the thickness δ is increased from $0.1a$ to $1.6a$. Here, eight mesh grids of different thicknesses δ are used. Examples of such meshes are depicted in Figures 18 and 19.

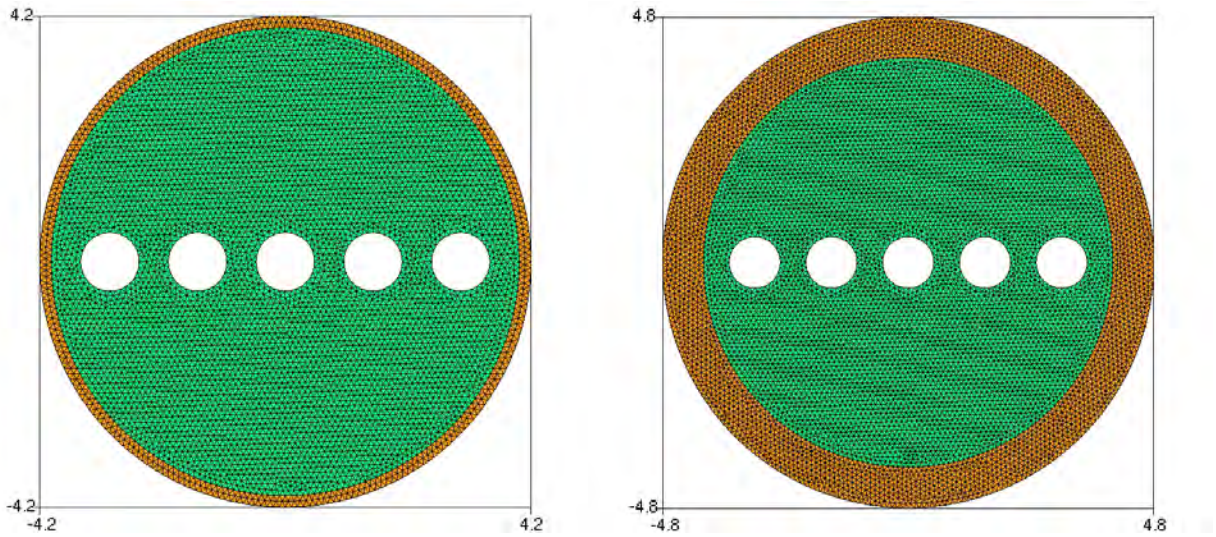

Figure 18: Typical rPML mesh grids used in the multiple scattering benchmark: (left) $\delta = 0.4a$ and $h = 0.3a$; (right) $\delta = 1.6a$ and $h = 0.28a$.

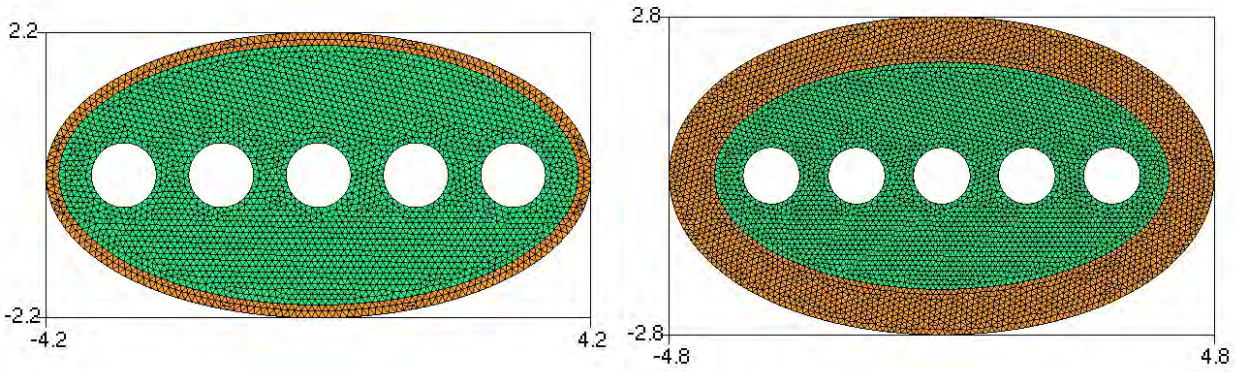

Figure 19: Typical ePML mesh grids used in the multiple scattering benchmark: (left) $\delta = 0.4a$ and $h = 0.3a$; (right) $\delta = 1.6a$ and $h = 0.28a$.

Table 1 reports the L^2 error with both rPML and ePML, corresponding to increasing values of the layer thickness δ, for two wavenumbers: $ka = 2.5\pi$ and $ka = 5\pi$. The polynomial order p and the absorption parameter R_0 are set equal to 8 and 10^{-10}, respectively. The results shown in Table 1 indicate that rPML and ePML lead, for practically comparable levels of the wave resolution τ_λ, to a similar accuracy. However, ePML involves about half of the total number n_{dof} of DoF used with the rPML. On the other hand, accurate results can be obtained by taking only $\delta \simeq \lambda$

	rPML			ePML		
δ	n_{dof}	τ_λ	$\epsilon_2[\%]$	n_{dof}	τ_λ	$\epsilon_2[\%]$
$\lambda/4$	129,316	21.13	0.00461	61,512	21.54	0.00140
$\lambda/2$	134,744	21.57	0.00020	65,386	22.21	0.00027
λ	151,820	22.89	0.00019	76,177	23.97	0.00025
1.5λ	165,574	23.91	0.00019	87,203	25.65	0.00025
2λ	180,054	24.93	0.00019	98,038	27.19	0.00025
δ						
$\lambda/4$	134,272	10.76	0.00534	64,481	11.03	0.00201
$\lambda/2$	129,316	10.56	0.00694	61,512	10.77	0.00191
λ	134,744	10.78	0.00012	65,386	11.11	0.00012
1.5λ	145,864	11.22	0.00009	70,888	11.56	0.00011
2λ	151,820	11.45	0.00009	76,177	11.98	0.00010

Table 1: The L^2 error corresponding to the rPML and ePML with respect to the layer thickness δ, with $p = 8$: (top) $ka = 2.5\pi$; (bottom) $ka = 5\pi$.

6.4.2 Influence of the absorption parameter R_0

The next numerical experiments focus on the effect of the absorption parameter R_0 on accuracy. Now, the layer thickness δ is set equal to $0.4a$. The rPML and ePML mesh grids used are those given in Figures 18 and 19 (left). Let us notice that in the case where $R_0 = 1$, rPML and ePML are equivalent to the zeroth-order absorbing boundary condition (3.16).

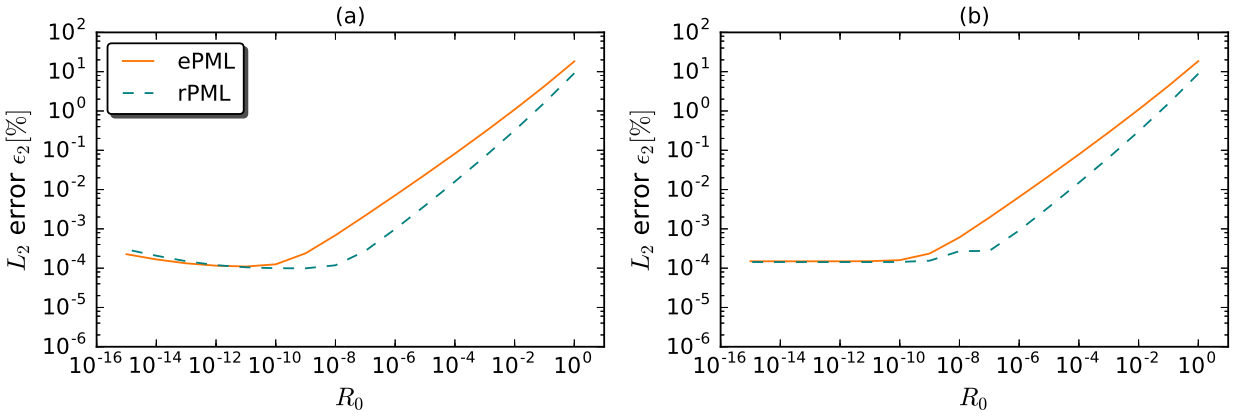

Figure 20: The L^2 error versus R_0: (a) $ka = 5\pi$ and $p = 8$; (b) $ka = 10\pi$ and $p = 12$.

In Figure 20, the relative L^2 error is plotted against the absorption parameter R_0, for the two wavenumbers $ka = 5\pi$ and $ka = 10\pi$. The polynomial order p is taken equal to 8 and 12, respectively. At the wavenumber $ka = 10\pi$, the rPML and ePML mesh grids involve elements which may contain up to $h/\lambda \simeq 1.3$ and $h/\lambda \simeq 1.5$ wavelengths, respectively.

The results presented in Figure 20 show an exponential decrease of the L^2 error ϵ_2 as the magnitude σ_0 of the absorption function σ (defined by Equation 3.18) increases. Furthermore, rPML and ePML give a similar L^2 error, when the parameter R_0 is sufficiently small. It can also be observed that below a small threshold R_0^*, i.e. $R_0 < R_0^*$, the L^2 error ϵ_2 becomes small and nearly constant. In contrast to the case of PML with low order FEM, when it is required to find an optimal value of the parameter σ_0 for a given mesh grid [37], a fixed sufficiently large value of σ_0

can be used here for different computational meshes, polynomial orders and wavenumbers, as can be already seen from the results of the single scattering benchmark where h and p convergences are studied, and R_0 is set equal to 10^{-10}. Of course, the L^2 error with rPML is lower, for large values of R_0 where numerical reflections are more pronounced, because its artificial boundary Σ is far from the scatterers compared to that of ePML.

6.4.3 Effect of the frequency

Now, rPML and ePML are compared against rBGT$_2$ and eBGT$_2$, respectively. The parameters δ and R_0 are chosen such that $\delta = 0.4a$ and $R_0 = 10^{-10}$. The mesh grids used in these numerical experiments, with rPML and ePML, are shown in Figures 18 and 19 (left), respectively. Those of rBGT$_2$ and eBGT$_2$ are deduced by removing the PML. To assess whether the performance of rPML or ePML is not affected by the frequency, wavenumbers ranging from $ka = 5\pi$ to 20π are considered. Figure 21 shows the relative L_2 error ϵ_2 against the number τ_λ of DoF per wavelength, for both rPML and rBGT$_2$ and two polynomial orders $p = 8$ and $p = 12$.

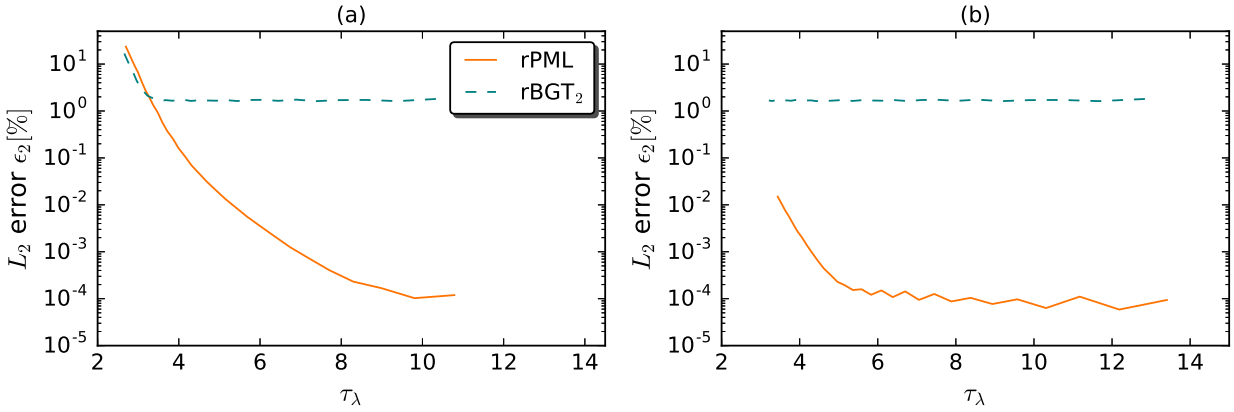

Figure 21: The L^2 error versus τ_λ: (a) $p = 8$; (b) $p = 12$.

The results shown in Figure 21(a) indicate that rPML and rBGT$_2$ perform similarly at a low wave resolution. As the wavenumber ka decreases, the wave becomes well resolved and a decay of the L^2 error with rPML is clearly seen, while it stagnates with rBGT$_2$. By increasing further the approximation order p, such that $p = 12$, the wave resolution τ_λ improves and a decay of the L^2 error with rPML can be observed from the results in Figure 21(b), especially for large wavenumbers. However, the L^2 error with rBGT$_2$ remains always higher than 1%.

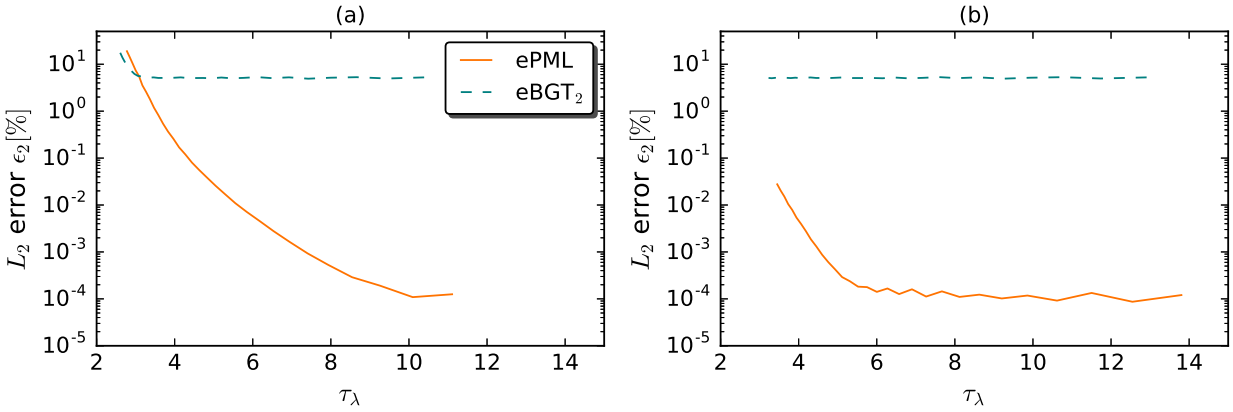

Figure 22: The L^2 error versus τ_λ: (a) $p = 8$; (b) $p = 12$.

Similarly, results using ePML and eBGT$_2$ are shown in Figure 22 and the trends described above are again seen. It can be concluded from this numerical study that the BGT$_2$ based ABCs are not suitable for multiple scattering applications.

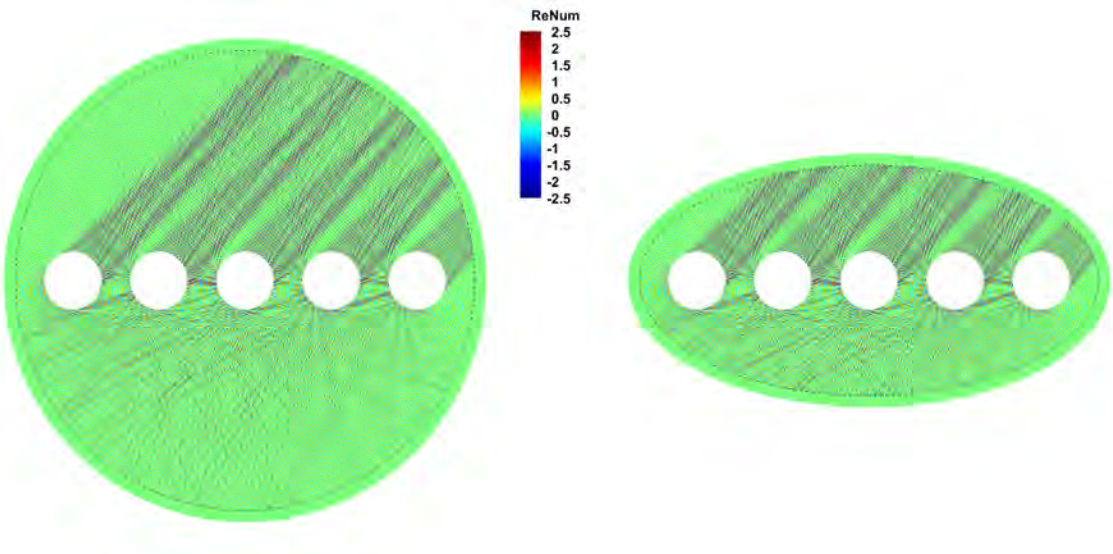

Figure 23: Real part of the diffracted potential for the wavenumber $ka = 20\pi$, with $p = 12$: (left) rPML solution, $\epsilon_2 = 0.015\%$ and $n_{\text{dof}} = 208,168$; (right) ePML solution, $\epsilon_2 = 0.027\%$ and $n_{\text{dof}} = 100,990$.

For illustration purposes, contour plots of the real parts of the rPML and ePML numerical solutions are depicted in Figure 23, for the wavenumber $ka = 20\pi$ with $p = 12$. It is worth noticing that elements of the used rPML and ePML mesh grids may contain up to $h/\lambda \simeq 2.65$ and $h/\lambda \simeq 3.02$ wavelengths, respectively. Good quality results are obtained, with only $\tau_\lambda \simeq 3.45$ for rPML and ePML. Moreover, the same level of accuracy is achieved using ePML, with a low computational effort.

7 Conclusions

The concept of curvilinear PMLs has been applied for short wave scattering computations in the frequency domain, using Bézier-Bernstein based finite elements. A key idea to obtain an efficient PML is the use of high order FEs on computational mesh grids consisting of large elements compared to the wavelength, to accurately resolve the PML. The blending map of Gordon and Hall is very useful for such applications in representing curved geometries. Standard FEMs face a trade-off between using a costly PML allowing a high absorption that minimizes the reflection of outgoing waves and a PML with a low absorption that is computationally cheaper to resolve. Intensive simulations have been carried out to assess the performance of the proposed PMLs. Comparison studies against a radial shaped second order ABC, dealing with Hankel source radiation and wave scattering by a rigid cylinder revealed that the radial PML enables the recovery of the predicted exponential and algebraic convergence rates of the p and h versions of BBFEM, respectively. For the scattering problem, where the wave involves many modes, the radial ABC leads to a similar performance, provided an accurate solution is not sought. Numerical results from multiple scattering problem by many rigid cylinders indicated that radial and elliptical shaped PMLs are able to provide very accurate results. The study highlighted the importance of elliptical shaped PMLs in reducing the size of the computational domain. Most notably, since BBFEM is able to efficiently capture the rapid decay of outgoing waves in the layer, the parabolic absorption function does not require a non trivial optimization procedure. Moreover, optimal performance can be achieved by using λ-thick PMLs. In general, it can be concluded that there is no need to tune the PML parameters for each problem; they worked well for wide ranges of frequencies, grid resolutions and polynomial orders. Recent works [20,39,40,62] have shown that PMLs based on unbounded absorption functions have a superior performance. A comparative study in this direction, using high order FEs is of a relevant importance in future investigations. Curvilinear PMLs can be readily extended to three-dimensional applications, as already done in Reference [64] for time domain wave problems. A model based on curved tetrahedral Bézier-Bernstein FEs is under development. To take advantage of high order methods, hp-refinement (see for instance [67]) is a promising strategy to further improve computational efficiency. It is worth noting that radial and elliptical shaped PMLs, combined to an efficient high-order FE solver, are well suited for time-domain wave problems, because they do not involve corners which require special treatment to avoid long time instabilities [31]. Many questions remain open, in particular, it would be interesting to extend the present method to time-dependent wave problems using the complex coordinate stretch technique in conjunction with the uniaxial PML concept [32, 64] and an appropriate high-order time stepping procedure.

A Appendix

In the orthogonal coordinate system (ζ_1, ζ_2) the gradient and divergence of a function u and a vector field $\boldsymbol{q} = q_1\boldsymbol{n} + q_2\boldsymbol{t}$ are given by

$$\boldsymbol{\nabla} u = \frac{1}{s_1}\frac{\partial u}{\partial \zeta_1}\boldsymbol{n} + \frac{1}{s_2}\frac{\partial u}{\partial \zeta_2}\boldsymbol{t} \tag{A.1}$$

$$\boldsymbol{\nabla}\cdot\boldsymbol{q} = \frac{1}{s_1 s_2}\left[\frac{\partial (s_2 q_1)}{\partial \zeta_1} + \frac{\partial (s_1 q_2)}{\partial \zeta_2}\right]. \tag{A.2}$$

Let us set

$$a = \frac{\hat{s}_1\hat{s}_2}{s_1 s_2}, q_1 = \frac{\hat{s}_2}{\hat{s}_1 s_2}\frac{\partial u}{\partial \zeta_1}, q_2 = \frac{\hat{s}_1}{s_1\hat{s}_2}\frac{\partial u}{\partial \zeta_2} \quad \text{and} \quad \boldsymbol{q} = q_1\boldsymbol{n} + q_2\boldsymbol{t}. \tag{A.3}$$

Then

$$\frac{1}{\hat{s}_1\hat{s}_2}\left[\frac{\partial}{\partial\zeta_1}\left(\frac{\hat{s}_2}{\hat{s}_1}\frac{\partial u}{\partial\zeta_1}\right)+\frac{\partial}{\partial\zeta_2}\left(\frac{\hat{s}_1}{\hat{s}_2}\frac{\partial u}{\partial\zeta_2}\right)\right] = \frac{1}{as_1s_2}\left[\frac{\partial(s_2q_1)}{\partial\zeta_1}+\frac{\partial(s_1q_2)}{\partial\zeta_2}\right] \tag{A.4}$$

$$= \frac{1}{a}\boldsymbol{\nabla}\cdot\boldsymbol{q}. \tag{A.5}$$

Since $q_1 = \dfrac{s_1\hat{s}_2}{\hat{s}_1s_2}\boldsymbol{\nabla}u\cdot\boldsymbol{n}$ and $q_2 = \dfrac{\hat{s}_1s_2}{s_1\hat{s}_2}\nabla u\cdot\boldsymbol{t}$, it follows that

$$\frac{1}{a}\boldsymbol{\nabla}\cdot\boldsymbol{q} = \frac{1}{a}\boldsymbol{\nabla}\cdot\left[\frac{s_1\hat{s}_2}{\hat{s}_1s_2}(\boldsymbol{\nabla}u\cdot\boldsymbol{n})\boldsymbol{n}+\frac{\hat{s}_1s_2}{s_1\hat{s}_2}(\nabla u\cdot\boldsymbol{t})\boldsymbol{t}\right] \tag{A.6}$$

$$= \frac{1}{a}\boldsymbol{\nabla}\cdot(\boldsymbol{A}\nabla u), \tag{A.7}$$

with the matrix $\boldsymbol{A}$ given by

$$\boldsymbol{A} = \frac{s_1\hat{s}_2}{\hat{s}_1s_2}\boldsymbol{n}\otimes\boldsymbol{n}+\frac{\hat{s}_1s_2}{s_1\hat{s}_2}\boldsymbol{t}\otimes\boldsymbol{t}. \tag{A.8}$$

As $\dfrac{s_1\hat{s}_2}{\hat{s}_1s_2} = \dfrac{\hat{\gamma}}{\gamma}$, the matrix A can be written as

$$\boldsymbol{A} = \frac{\hat{\gamma}}{\gamma}\boldsymbol{n}\otimes\boldsymbol{n}+\frac{\gamma}{\hat{\gamma}}\boldsymbol{t}\otimes\boldsymbol{t}. \tag{A.9}$$

Moreover, we have

$$a = \frac{\hat{s}_1\hat{s}_2}{s_1s_2} = \hat{\gamma}\gamma. \tag{A.10}$$

A.1 Radial shaped PML

Suppose that the fictitious interface Σ is a circle of radius ρ centred at the origin and described by its parametric equation

$$\boldsymbol{p} = (\rho\cos\theta,\rho\sin\theta)^\top \quad \text{with} \quad \theta\in[0,2\pi]. \tag{A.11}$$

The unit vectors $\boldsymbol{t}$ and $\boldsymbol{n}$ are given by

$$\boldsymbol{t} = (\cos\theta,\sin\theta)^\top \quad \text{and} \quad \boldsymbol{n} = (-\sin\theta,\cos\theta)^\top. \tag{A.12}$$

In this case we take $\zeta_1 = r-\rho$, $\zeta_2 = \rho\theta$, where $r = |\boldsymbol{x}|$. The curvature of Σ is given by $\kappa = \frac{1}{\rho}$ and $\hat{\sigma}$ can be written as

$$\hat{\sigma} = \frac{1}{r}\int_0^{r-\rho}\sigma(s)\mathrm{d}s. \tag{A.13}$$

The matrix $\boldsymbol{A}$ becomes

$$\boldsymbol{A} = \begin{bmatrix} \dfrac{\hat{\gamma}}{\gamma}\cos^2\theta+\dfrac{\gamma}{\hat{\gamma}}\sin^2\theta & \left(\dfrac{\hat{\gamma}}{\gamma}-\dfrac{\gamma}{\hat{\gamma}}\right)\cos\theta\sin\theta \\ \left(\dfrac{\hat{\gamma}}{\gamma}-\dfrac{\gamma}{\hat{\gamma}}\right)\cos\theta\sin\theta & \dfrac{\gamma}{\hat{\gamma}}\cos^2\theta+\dfrac{\hat{\gamma}}{\gamma}\sin^2\theta \end{bmatrix}. \tag{A.14}$$

A.2 Elliptical shaped PML

Suppose now that the fictitious interface Σ is an ellipse centred at the origin with semi-major and semi-minor axes denoted respectively by ρ_1 and ρ_2. The parametric representation of Σ is given by

$$\boldsymbol{p} \;=\; (\rho_1 \cos\theta, \rho_2 \sin\theta)^\top, \quad \text{with} \quad \theta \in [0, 2\pi]. \tag{A.15}$$

The distance from a point $\boldsymbol{x}$ in the PML to the ellipse Σ given by ζ_1, is usually computed based on a numerical algorithm. Here, as previously mentioned, Newton's method is used. The element arc length $\mathrm{d}\zeta_2$ can be written as

$$\mathrm{d}\zeta_2 \;=\; \left|\frac{\partial \boldsymbol{p}}{\partial \theta}\right| \mathrm{d}\theta \tag{A.16}$$

$$\;=\; \sqrt{\rho_1^2 \sin^2\theta + \rho_2^2 \cos^2\theta}\; \mathrm{d}\theta. \tag{A.17}$$

Hence to obtain the arc length ζ_2, it is required to evaluate an elliptic integral. The curvature of Σ is defined by Formula (6.6). The unit vectors $\boldsymbol{t}$ and $\boldsymbol{n}$ are given by

$$\boldsymbol{t} \;=\; \frac{\partial \boldsymbol{p}}{\partial \theta}\frac{\mathrm{d}\theta}{\mathrm{d}\zeta_2} \tag{A.18}$$

$$\;=\; \frac{1}{\sqrt{\rho_1^2 \sin^2\theta + \rho_2^2 \cos^2\theta}}(-\rho_1 \sin\theta, \rho_2 \cos\theta)^\top, \tag{A.19}$$

$$\boldsymbol{n} \;=\; \frac{1}{\sqrt{\rho_1^2 \sin^2\theta + \rho_2^2 \cos^2\theta}}(\rho_2 \cos\theta, \rho_1 \sin\theta)^\top. \tag{A.20}$$

In the same fashion as before, we have

$$\boldsymbol{A} \;=\; \frac{\hat{\gamma}}{\gamma}\boldsymbol{n}\otimes\boldsymbol{n} + \frac{\gamma}{\hat{\gamma}}\boldsymbol{t}\otimes\boldsymbol{t} \tag{A.21}$$

$$\;=\; \frac{1}{\rho_1^2 \sin^2\theta + \rho_2^2 \cos^2\theta}\begin{bmatrix} \dfrac{\hat{\gamma}}{\gamma}\rho_2^2\cos^2\theta + \dfrac{\gamma}{\hat{\gamma}}\rho_1^2\sin^2\theta & \left(\dfrac{\hat{\gamma}}{\gamma} - \dfrac{\gamma}{\hat{\gamma}}\right)\rho_1\rho_2\cos\theta\sin\theta \\ \left(\dfrac{\hat{\gamma}}{\gamma} - \dfrac{\gamma}{\hat{\gamma}}\right)\rho_1\rho_2\cos\theta\sin\theta & \dfrac{\hat{\gamma}}{\gamma}\rho_1^2\sin^2\theta + \dfrac{\gamma}{\hat{\gamma}}\rho_2^2\cos^2\theta \end{bmatrix}. \tag{A.22}$$

References

[1] J. Bérenger, A perfectly matched layer for the absorption of electromagnetic waves. *J. Comput. Phys.* 114 (1994) 185–200.

[2] I. Harari, A survey of finite element methods for time-harmonic acoustics. *Comput. Methods Appl. Mech. Eng.* 195 (13–16) (2006) 1594–1607, a Tribute to Thomas J. R. Hughes on the Occasion of his 60th Birthday.

[3] D. Komatitsch, R. Martin, An unsplit convolutional perfectly matched layer improved at grazing incidence for the seismic wave equation. *Geophysics.* 72 (5) (2007) SM155–SM167.

[4] D. Komatitsch, J. Tromp, A perfectly matched layer absorbing boundary condition for the second-order seismic wave equation. *Geophys. J. Int.* 154 (1) (2003) 146–153.

[5] R. Martin, D. Komatitsch, A. Ezziani. An unsplit convolutional perfectly matched layer improved at grazing incidence for seismic wave equation in poroelastic media. *Geophysics* 73(4) (2008) T51–T61.

[6] W. C. Chew, Q. H. Liu, Perfectly matched layers for elastodynamics: A new absorbing boundary condition. J. Comput. Acoust. 4 (4) (1996) 341–359.

[7] E. Bécache, S. Fauqueux, P. Joly, Stability of perfectly matched layers, group velocities and anisotropic waves. *J. Comput. Phys.* 188 (2) (2003) 399–433.

[8] F. Collino, C. Tsogka, Application of the perfectly matched absorbing layer model to the linear elastodynamic problem in anisotropic heterogeneous media. *Geophysics* 66 (1) (2001) 294–307.

[9] U. Basu, A.K. Chopra, Perfectly matched layers for time-harmonic elastodynamics of unbounded domains: theory and finite-element implementation, Comput. *Methods Appl. Mech. Engrg.* 192 (11–12) (2003) 1337–1375.

[10] I. M. Navon, B. Neta, M.Y. Hussaini, A perfectly matched layer approach to the linearized shallow water equations models, *Mon. Weather Rev.* 132 (6) (2004) 1369–1378.

[11] J. W. Lavelle, W. C. Thacker, A pretty good sponge: Dealing with open boundaries in limited-area ocean models. *Ocean Modell.* 20 (3) (2008) 270–292.

[12] A. Bayliss, E. Turkel, Radiation boundary conditions for wave-like equations, *Commun. Pure Appl. Math.* 33 (1980) 707–725.

[13] A. Bayliss, M. Gunzburger, E. Turkel, Boundary conditions for the numerical solution of elliptic equations in exterior regions. *SIAM J. Appl. Math.* 42 (1982) 430–451.

[14] B. Engquist, A. Majda, Absorbing boundary conditions for the numerical simulation of waves. *Math. Comput.* 31 (1977) 629–651.

[15] B. Engquist, A. Majda, Radiation boundary conditions for acoustic and elastic wave calculations. *Commun. Pure Appl. Math.* 32 (1979) 313–357.

[16] F. Kang, Finite element method and natural boundary reduction. *In: Proceedings of the International Congress of Mathematics, Warsaw*, 1983, 1439–1453.

[17] J. B. Keller, D. Givoli, Exact non-reflecting boundary conditions. *J. Comput. Phys.* 82 (1989) 172–192.

[18] J. J. Shirron, I. Babuška, A comparison of approximate boundary conditions and infinite element methods for exterior Helmholtz problems. *Comput. Methods Appl. Mech. Eng.* 164 (1998) 121–139.

[19] D. Givoli, T. Hagstrom, I. Patlashenko, Finite element formulation with high-order absorbing boundary conditions for time-dependent waves. *Comput. Methods Appl. Mech. Engrg.* 195 (2006): 3666–3690.

[20] D. Rabinovich, D. Givoli, E. Bécache . Comparison of high order absorbing boundary conditions and perfectly matched layers in the frequency domain. *Int. J. Numerical Methods in Biomedical Engineering.* 26 (2010) (10) 1351–1369.

[21] D. Givoli, Numerical Methods for Problems in Infinite Domains. *Elsevier: Amsterdam*, 1992.

[22] K. Ihlenburg, Finite Element Analysis of Acoustic Scattering. *Springer-Verlag, New York*, 1998.

[23] M. N. Guddati, J. L. Tassoulas, Continued-fraction absorbing boundary conditions for the wave equation. *J. Comput. Acoust.* 8 (2000) 139–156.

[24] D. Rabinovich, D. Givoli, J. Bielak, T. Hagstrom, The Double Absorbing Boundary method for a class of anisotropic elastic media. *Comput. Methods in Appl. Mech. and Eng.* 315 (2017) 190–221.

[25] P. Bettess, O. C. Zienkiewicz, Diffraction and refraction of surface waves using finite and infinite elements. *Int. J. Numer. Meth. Eng.* 11 (1977) 1271–1290.

[26] K. Gerdes, L. Demkowicz, Solution of 3D-Laplace and Helmholtz equations in exterior domains using hp-infinite elements, *Comput. Methods Appl. Mech. Engrg.* 137 (1996) 239–273.

[27] R. J. Astley, Wave envelope and infinite elements for acoustical radiation. *Intern. J. for Num. Methods in Fluids.* 3 (1983) 507–526.

[28] R. E. Kleinman, G.F. Roach, Boundary integral equations for the three-dimensional Helmholtz equation. *SIAM Rev.* 16 (2) (1974) 214–236.

[29] R. P. Shaw, Integral equation methods in acoustics, *in: C.A. Brebbia (Ed.), Boundary Elements X, vol. 4, Computational Mechanics Publications, Southampton.* (1988) 221–244.

[30] R. W. Ziolkowski, Time-derivative Lorentz material model-based absorbing boundary condition, *IEEE Trans. Antennas Propag.* 45 (10) (1997) 1530–1535.

[31] E. Bécache and A. Prieto. Remarks on the stability of cartesian PMLs in corners. *Applied Numerical Mathematics.* 62 (2012) (11) 1639–1653.

[32] W. C. Chew, W. H. Weedon, A 3D perfectly matched medium from modified Maxwells equations with stretched coordinates. *Microwave and Optical Technology Letters.* 7(13) (1994) 599–604.

[33] F. L. Teixeira, W. C. Chew, PML–FDTD in cylindrical and spherical grids. *IEEE Microwave Guided Wave Lett.* 7 (9) (1997) 285–287.

[34] F. L. Teixeira, W. C. Chew, Systematic derivation of anisotropic PML absorbing media in cylindrical and spherical coordinates, *IEEE Microwave Guided Wave Lett.* 7 (11) (1997) 371–373.

[35] F. L. Teixeira, W. C. Chew, Analytical derivation of a conformal perfectly matched absorber for electromagnetic waves. *Microw. Opt. Technol. Lett.* 17 (4) (1998) 231–236.

[36] F. Collino, P. Monk, The perfectly matched layer in curvilinear coordinates. *SIAM J. Sci. Comput.* 19 (1998) 2061–2090.

[37] F. Collino, P. Monk, Optimizing the perfectly matched layer. *Comput. Methods Appl. Mech. Engrg.* 164 (1998) 157–171.

[38] G. Bunting, A. Prakash, T. Walsh, C. Dohrmann, Parallel Ellipsoidal Perfectly Matched Layers for Acoustic Helmholtz Problems on Exterior Domains. *Journal of Theoretical and Computational Acoustics.* 26 (02) (2018) 1850015.

[39] A. Bermúdez, L. Hervella-Nieto, A. Prieto, R. Rodríguez, An exact bounded perfectly matched layer for time-harmonic scattering problems. *SIAM J. Sci. Comput.* 30 (1) (2007) 312–338.

[40] A. Bermúdez, L. Hervella-Nieto, A. Prieto, R. Rodríguez, An optimal perfectly matched layer with unbounded absorbing function for time-harmonic acoustic scattering problems. *J. Comput. Phys.* 223 (2007) 469–488.

[41] M. Lassas, J. Liukkonen, E. Somersalo, Complex Riemannian metric and absorbing boundary condition. *J. Math. Pures Appl.* 80 (7) (2001) 739–768.

[42] L. Zschiedrich, R. Klose, A. Schädle, F. Schmidt, A new finite element realization of the perfectly matched layer method for Helmholtz scattering problems on polygonal domains in two dimensions. *J. Comput. Appl. Math.* 188 (1) (2006) 12–32.

[43] P. J. Matuszyk, L. F. Demkowicz, Parametric finite elements, exact sequences and perfectly matched layers. *Comput. Mech.* 51 (1) (2013) 35–45.

[44] F. Ihlenburg, I. Babuška, Finite-element solution of the Helmholtz-equation with high wavenumber. Part I: the h-version of the FEM. *Computers and Mathematics with Applications.* 30 (1995) 9–37.

[45] F. Ihlenburg and I. Babuška, Finite element solution of the Helmholtz equation with high wavenumber. Part II: The h-p version of the FEM. *Siam Journal on Numerical Analysis.* 34 (1997) 315–358.

[46] I. Babuška, S. A. Sauter, Is the pollution effect of the FEM avoidable for the Helmholtz equation considering high wave numbers? *SIAM Review.* 42 (3) (2000) 451–484.

[47] S. Petersen, D. Dreyer, V. O. Estorff, Assessment of finite and spectral element shape functions for efficient iterative simulations of interior acoustics. *Comput. Methods Appl. Mech. Engrg.* 195 (44–47) (2006) 6463–6478.

[48] R. C. Kirby, K. T. Thinh, Fast simplicial quadrature–based finite element operators using Bernstein polynomials, *Numerische Mathematik.* 121(2) (2012) 261–279.

[49] M. Ainsworth, G. Andriamaro, O. Davydov, Bernstein-Bézier Finite Elements of Arbitrary Order and Optimal Assembly Procedures. *SIAM Journal on Scientific Computing.* 33 (2011) 3087–3109.

[50] M. Ainsworth, O. Davydov, L. L. Schumaker, Bernstein-Bézier finite elements on tetrahedral-hexahedral-pyramidal partitions. *Computer Methods in Applied Mechanics and Engineering.* **304** (2016) 140–170.

[51] A. Lieu, G. Gabard, H. Bériot, A comparison of high-order polynomial and wave-based methods for Helmholtz problems. *Journal of Computational Physics.* 321 (2016)105–125.

[52] H. Bériot, A. Prinn, G. Gabard, Efficient implementation of high-order finite elements for Helmholtz problems. *Int. J. Numer. Meth. Eng.* 106 (2015) 213–240.

[53] A. El Kacimi, O. Laghrouche, M.S. Mohamed, J. Trevelyan, Bernstein-Bézier based finite elements for efficient solution of short wave problems. *Comput. Methods Appl. Mech. Engrg.* 343 (2019) 166–185.

[54] K. Christodoulou, O. Laghrouche, M.S. Mohamed and J. Trevelyan. High-order finite elements for the solution of Helmholtz problems. *Computers & Structures.* 191 (2017) 129–139.

[55] I. Babuška, M. Griebel, J. Pitkaranta, The problem of selecting the shape functions for a p-type finite element, Internat. J. Numer. Methods Engrg. (1989) 1891–1908

[56] J. Melenk, S. Sauter, Convergence analysis for finite element discretizations of the Helmholtz equation with Dirichlet-to-Neumann boundary conditions. *Mathematics of Computation.* 79 (2010) 1871–1914.

[57] J. Melenk, S. Sauter, Wavenumber explicit convergence analysis for Galerkin discretizations of the Helmholtz Equation. *SIAM Journal on Numerical Analysis.* 49 (2011) 1210–1243.

[58] W. J. Gordon, C. A. Hall, Construction of Curvilinear Coordinate Systems and Applications to Mesh Generation. *Int. J. Num. Meth. in Engng.* 7 (1973) 461–77.

[59] W. J. Gordon, C. A. Hall. Transfinite Element Methods: Blending Function Interpolation over Arbitrary Curved Element Domains.*Numer. Math.* 21 (1973) 109–29.

[60] B. Szabo, I. Babuška, Finite Element Analysis. John Wiley & Sons, Inc, 1991.

[61] W. C. Chew, J. M. Jin, Perfectly matched layers in the discretized space: an analysis and optimization. *Electromagnetics.* 16 (1996) 325–340.

[62] A. Modave, E. Delhez, C. Geuzaine, Optimizing perfectly matched layers in discrete contexts. *nt. J. Numer. Meth. Engng.* 99 (6) (2014) 410–437.

[63] D. Colton, R. Kress, Inverse acoustic and electromagnetic scattering theory. *Springer*, 1992.

[64] A. Modave, J. Lambrechts, C. Geuzaine, Perfectly matched layers for convex truncated domains with discontinuous Galerkin time domain simulations. *J. Comput. Phys.* 73 (2017) 684–700.

[65] X. Antoine, H. Barucq, A. Bendali, Bayliss-Turkel-like radiation conditions on surfaces of arbitrary shape. *J. Math. Anal. Appl.* 229 (1) (1999)184–211.

[66] I. Harari, U. Albocher, Studies of FE/PML for exterior problems of time-harmonic elastic waves. *Comput. Methods Appl. Mech. Engrg.* 195 (2006) 3854–3879.

[67] C. Michler, L. Demkowicz, J. Kurtz, D. Pardo, Improving the performance of perfectly matched layers by means of hp-adaptivity. *Numerical Methods for Partial Differential Equations.* 23 (4) (2007) 832–858.

[68] X. Antoine, Fast approximate computation of a time-harmonic scattered field using the on-surface radiation condition method. *IMA J. Appl. Math.* 66 (2001) 83–110.

[69] M.J. Grote, J.B. Keller, On non-reflecting boundary conditions. *J. Comput. Phys.* 122 (1995) 231–243.

[70] G. Ben-Porat, D. Givoli, Solution of unbounded domain problems using elliptic artificial boundaries. *Commun. Numer. Meth. Eng.* 11 (1995) 735–741.

[71] R. C. Reiner, R. Djellouli, I. Harari, The performance of local absorbing boundary conditions for acoustic scattering from elliptical shapes.*Comput. Meth. Appl. Mech. Eng.* 195 (2006) 3622–3665.

[72] M. Medvinsky, E. Turkel, U. Hetmaniuk, Local absorbing boundary conditions for elliptical shaped boundaries. *J. Comput. Phys.* 227 (2008) 8254–8267.

[73] G. E. Karniadakis, S. J. Sherwin, Spectral/hp element methods for computational fluid dynamics, Numerical Mathematics and Scientific Computation. *Oxford University Press, New York*, 2005.

[74] P. Šolín, K. Segeth, I. Doležel, Higher-Order Finite Element Methods. *Chapman & Hall, New York*, 2003.

[75] P. R. Amestoy, I. S. Duff, J. Y. L'Excellent, Multifrontal parallel distributed symmetric and unsymmetric solvers.*Comput. Meth. Appl. Mech. Eng.* 184 (2–4) (2000) 501–520.

[76] C. M. Linton, D. V. Evans, The interaction of waves with arrays of vertical circular cylinders. *J. Fluid Mech.* 215 (1990) 549–69.

[77] R. Sevilla, S. Fernández-Méndez, A. Huerta, NURBSEnhanced Finite Element Method (NEFEM): a seamlessbridge between CAD and FEM.Arch, *Comput. Methods Engrg.*18(4) (2011) 441–484.

[78] V. S. Ziel, H. Bériot. O. Atak, G. Gabard, High-order 2D mesh curving methods with a piecewise linear target and application to Helmholtz problems. *Computer-Aided Design.* 105 (2018) 26–41.

[79] I. Harari, T. J. R. Hughes, Analysis of continuous formulations underlying the computation of time-harmonic acoustics in exterior domains. *Comput. Methods Appl. Mech. Engrg.* 97 (1) (1992) 103–124.

[80] M. S. Mohamed, O. Laghrouche, A. El Kacimi, Some numerical aspects of the PUFEM for efficient solution of 2D Helmholtz problems. *Computers & Structures.* 88 (23–24) (2010) 1484–1491.

[81] M. J. Grote, C. Kirsch, Dirichlet-to-Neumann boundary conditions for multiple scattering problems. *J. Comput. Phys.* 201 (2004) 630–650.

[82] X. Jiang, W. Zheng, Adaptive perfectly matched layer method for multiple scattering problems. *Comput. Methods Appl. Mech. Engrg.* 201–204 (2012) 42–52.

[83] C. Geuzaine, J. F. Remacle, Gmsh: A 3D finite element mesh generator with built-in pre-and post-processing facilities. *Internat. J. Numer. Methods Engrg.* 79 (11) (2009) 1309–1331.

[84] P. G. Petropoulos, Reflectionless Sponge layers as absorbing boundary conditions for the numerical solution of Maxwell equations in rectangular, cylindrical, and spherical coordinates. *SIAM J. Appl. Math.* 60 (3) (2000) 1037–1058.

[85] X. Antoine, M. Darbas, Y. Y. Lu, An improved surface radiation condition for high-frequency acoustic scattering problems. *Comput. Methods Appl. Mech. Engrg.* 195 (2006) 4060–4074.

[86] A. Pierce, Acoustics: An Introduction to Its Physical Principles and Applications. *Acoustical Society of America*, 1989.